Physics of Fluids

The role of breakup and coalescence in fine-scale bubble-induced turbulence: part II - kinematics

Accepted Manuscript: This article has been accepted for publication and undergone full peer review but has not been through the copyediting, typesetting, pagination, and proofreading process, which may lead to differences between this version and the Version of Record.

Cite as: Physics of Fluids (in press) (2022); https://doi.org/10.1063/5.0100334
Submitted: 23 May 2022 • Accepted: 02 August 2022 • Accepted Manuscript Online: 04 August 2022

Immanuvel Paul, Bruño Fraga, Michael S. Dodd, et al.

View Online Export Citation CrossMark

ARTICLES YOU MAY BE INTERESTED IN

The role of breakup and coalescence in fine-scale bubble-induced turbulence: Part I - dynamics
Physics of Fluids (2022); https://doi.org/10.1063/5.0094573

Perspectives on the importance of complex systems in understanding our climate and climate change—The Nobel Prize in Physics 2021
Chaos: An Interdisciplinary Journal of Nonlinear Science **32**, 052102 (2022); https://doi.org/10.1063/5.0090222

A density scaling conjecture for aging glasses
The Journal of Chemical Physics **157**, 054503 (2022); https://doi.org/10.1063/5.0090869

© 2022 Author(s).

Accepted to Phys. Fluids 10.1063/5.0100334

The role of breakup and coalescence in fine-scale bubble-induced turbulence: part II - kinematics

I. Paul,[1, a)] B. Fraga,[2] M. S. Dodd,[3] and C. Lai[4]
[1)] *School of Engineering, Newcastle University, Newcastle upon Tyne, United Kingdom - NE1 7RU*
[2)] *Department of Civil Engineering, University of Birmingham, Birmingham, United Kingdom - B15 2TT*
[3)] *Center for Turbulence Research, Stanford University, Stanford, California, USA 94305*
[4)] *School of Civil and Environmental Engineering, Georgia Institute of Technology, Atlanta, Georgia, USA 30332*

(Dated: 25 July 2022)

This second part of the research explores the kinematic aspect of fine-scale bubble-induced turbulence (BIT) to (i) present the effect of bubble breakup and coalescence and (ii) compare it against the universal kinematic fine-scale turbulence characteristics reported in the literature. To this end, we simulate a dilute bubbly system of 0.5% void fraction using two distinct numerical simulations. In the volume of fluid (VoF) simulation, bubbles undergo breakup and coalescence. In the immersed boundary method (IBM) simulation, however, they act as rigid spheres. We also perform a simulation of classical homogeneous isotropic turbulence (HIT). The first important outcome of this study is that BIT is radically different from HIT in terms of its kinematic fine-scale characteristics. In the vorticity-dominating regions, BIT exhibits a weak vortex stretching. This weak vortex stretching is due to (a) the intermediate strain-rate eigenvalues skewed weakly to positive and (b) the extensive strain-rate eigenvector aligning perpendicular to the vorticity vector. The BIT has, on average, not only a weak enstrophy production but also a weak strain production in strain-dominating regions. The weak strain production is due to (a) the presence of vortex stretching in highly-strained fluid elements and (b) the absolute magnitude of compressive strain-rate eigenvalue being as close to the extensive strain-rate eigenvalue. Thus, none of the kinematic fine-scale HIT characteristics is noted for BIT. The second important conclusion is that bubble breakup and coalescence play little to no influence on the kinematics of fine-scale BIT as VoF and IBM simulations produce similar results.

I. INTRODUCTION

Classical turbulence informs us that turbulent flows consist of scales of various sizes. These scales range from the largest to the smallest sizes and the turbulent kinetic energy cascades from the largest to the smallest. The largest scale is called the integral length scale in which most of the kinetic energy of turbulence resides. The large scales of turbulence are often influenced by boundary conditions of the problem and as such, they seldom exhibit universal characteristics. On the other hand, the smallest length scale in turbulence is called the Kolmogorov length scale at which the turbulent kinetic energy is dissipated. The fine scales of turbulence are free from the influences of initial and boundary conditions and they are also isotropic. These attractive characteristics not only lead to mathematical simplification of turbulent small scales problem but also universal theories of turbulence. Our main objective in this two-part research is to reveal the universal aspects of bubble-induced fine-scale turbulence.

To understand the characteristics of turbulent small scales, it is useful to imagine that fluid is nothing but a collection of infinite infinitesimal fluid elements. We know that the governing equations of fluid flow are obtained by taking one of these infinitesimal fluid elements and applying the fundamental conservation laws. When we apply the momentum conservation principle to such an infinitesimal fluid element, we note that at least four forces are acting on a fluid element. The first is the force due to local acceleration. The second one is the force due to convective acceleration. Forces due to local and convective accelerations are collectively known as inertial forces. The third one is the pressure force and the final one is the viscous force. Apart from these, there are also body forces. It is easy to prove that the inertial forces create steep gradients of velocity in the turbulent flow and the viscous forces try to annihilate such steep gradients. The consequence of these forces is that each fluid element is now left with the ability to rotate and deform. In other words, each fluid element now contains vorticity and strain and they interact with each other in a complex nonlinear way.

This physical intuition explained in the above paragraph can also be obtained mathematically. We know that the large scales contain most of the turbulent kinetic energy. Therefore, the right mathematical term that represents the large scales must be in terms of velocity fluctuations (for instance, turbulent kinetic energy). We also know that small scales dissipate the turbulent kinetic energy. Therefore, the meaningful mathematical representation of small scales can only be in terms of velocity gradients (for example, dissipation, vorticity, strain etc). This would lead to conclude that the velocity gradient tensor (VGT) is the ideal quantity to study fine-scale turbulence. When we decompose the VGT, we note that

[a)] Electronic mail: immanuvel.paul@newcastle.ac.uk

Accepted to Phys. Fluids 10.1063/5.0100334

it comprises symmetric and anti-symmetric parts which are nothing but strain and vorticity. Thus, we have seen from the mathematical principles also that a fine-scale fluid element consists of vorticity and strain.

In general, there are two ways to study fine-scale turbulence. First, we can study by tracking an individual fluid element for its dynamics. This is what was carried out and presented in the first part of this research. In the dynamical study, we take into effect all the forces acting on the fluid element as it evolves in time. In the second method of studying fine-scale turbulence, we collect a large sample of fluid elements and then carry out a statistical study on them. Such a study is kinematic as we do not consider the forces acting on the fluid element. This kinematic study would reveal, on average, whether strain or vorticity is dominating at the location/domain of interest. It would also tell us about the topology of strain- and vorticity-dominated regions locally within the location/domain of interest. That is why this kinematic study of fine-scale turbulence is often called the topological study of fine-scale turbulence.

The topological study of fine-scale homogeneous isotropic turbulence (HIT) was carried out first by Perry and Chong [1] and Chong, Perry, and Cantwell [2]. These studies revealed the following universal characteristics of the fine-scale HIT: (i) the magnitude of vorticity, on average, is twice that of strain, (ii) vortex stretching, on average, is preferred over vortex compression, (iii) the value of strain self-amplification, on average, is positive, (iv) the vorticity-dominating region in the flow are made up of tube-like structures, (v) the strain-dominating or dissipating regions are comprised of sheet-like structures, (vi) the intermediate strain-rate eigenvalue, on average, is positive and (vii) the vorticity vector aligns strongly with the intermediate strain-rate eigenvector and aligns weakly with the extensive strain-rate eigenvector. These universal results have been widely reported in variety of flow configurations such as HIT[3], boundary layer[4], grid turbulence[5] and mixing layer[6].

Exploring the literature on bubble-induced turbulence (BIT), we see that only a handful of studies carried out on the topological aspects of it despite a large collection of experimental and numerical studies of multiphase flow[7–23]. Hasslberger, Klein, and Chakraborty [24] performed direct numerical simulation (DNS) of two air bubbles suspended in a water column. They found a higher volume fraction of flow topologies in the dispersed phase compared to the surrounding continuous phase. They argued that their observation is due to the high production of vorticity at the curvatures. Dodd and Jofre [25] studied the topology of multiphase turbulence for decaying isotropic turbulence laden with finite-size droplets. Their study mainly focused on studying flow topology concerning the distance from the droplet surface. They found that the topological results on the surface of the droplet are remarkably similar to the viscous sub-layer of wall turbulence. Bubbles in a turbulent channel flow were investigated for their topological nature by[26]. They found a significant difference between the topologies of the dispersed and continuous phases. They also found a preference for higher dissipation near the bubble surface while high enstrophy events are preferred away from the bubble. Very recently, Hasslberger *et al.* [27] also studied the bubbly wall turbulent flows to show that the topologies of the dispersed and continuous phases are different. There are also topological studies on vaporising and surfactant-laden bubbles[28–30].

Summarising from the above discussion, the main theme of topological studies in multiphase turbulence has been to elucidate how much the flow topology varies from the dispersed phase to the continuous phase. To the best of the authors' knowledge, there has not been any study focused on a detailed comparison of the topological characteristics for BIT with that of the classical HIT. Therefore, our first objective is to explore the aforementioned seven kinematic characteristics of BIT and then compare them with that of HIT to see how similar/different BIT is to HIT. Our second objective is to reveal how much the bubble breakup and coalescence influence the fine scales of BIT. To meet these two objectives, we carry out dilute bubbly turbulent flows of a void fraction of 0.5%. This particular value of void fraction was chosen so that there will be a clearer -3 slope in the energy spectrum as noted in the experiments[7–14]. We simulate this system using two different numerical solvers. In the volume of fluid (VoF) solver, the bubbles undergo breakup and coalescence. On the other hand, the immersed boundary method (IBM) solver treats the bubbles as rigid spheres. For these two simulations, we carry out the topological study of BIT and compare the results between the simulations and with the results of HIT. To make sure we have developed the right postprocessing tools, we also simulate HIT. The paper is organised as follows. The next section presents the numerical details. Section III presents the main results of this study where we look for the seven universal kinematic characteristics of HIT in BIT. Finally, the results are summarised in section IV.

II. NUMERICAL DETAILS

Direct numerical simulation (DNS) of the continuous liquid matrix is performed by solving the Navier-Stokes equations for an unsteady, incompressible and viscous flow. The dispersed phase (bubbles) is solved using two fundamentally different techniques: the volume of fluid method (VoF) and the immersed boundary method (IBM). The former allows bubble deformability, break-up and coalescence, unlike the latter which considers each bubble a rigid sphere. The bubble swarm was simulated in a periodic vertical channel ($40D_0$x$20D_0$x$20D_0$, where D_0 is the initial bubble diameter) in which the bubble's buoyancy is the only source of motion. The Reynolds number associated to the bubble size is $Re_p \approx 400$ and the gravity acceleration is $\mathbf{g} = -9.81ms^{-2}$. A void fraction of 0.5% was simulated for both IBM and VoF. Simu-

Accepted to Phys. Fluids 10.1063/5.0100334

lations of Homogeneous Isotropic turbulence (HIT) have been performed in a $2\pi \times 2\pi \times 2\pi$ periodic box with 128 mesh points along each direction. The Reynolds number based on the Taylor length scale is Re_λ=80 for the HIT case.

For further details on the governing equations, numerical methodologies and model setups, we kindly refer the reader to part one of this research where a detailed explanation is presented[31].

III. RESULTS AND DISCUSSION

This section presents the main results of this study. We first discuss the velocity gradient kinematics in terms of various joint probability distributions of its invariants. Then, we take up the production terms of the VGT and discuss the factors affecting these terms. Note that the joint probability distributions (JPDFs) and probability distributions (PDFs) of various velocity gradient quantities are studied only for the continuous phase in this study. As with the first part, here also we focus our attention on two temporal locations. One is the time instant at which the best possible -3 slope is observed in the energy spectrum where the flow is unsteady as the turbulent kinetic energy continues to increase at this time instant. We call this location US_{-3} which corresponds to the simulation time of $t = 3s$ and $0.5s$ in VoF and IBM respectively. The second time instant is in the quasi-steady region of flow where the turbulent kinetic energy remains almost unchanged with respect to time and the -3 slope in the energy spectrum. We designate this second location as QS_{-3} which corresponds to $t = 18s$ and $3.5s$ in VoF and IBM simulations respectively.

A. Flow topology

We can write the velocity gradient tensor (VGT) $A_{ij} = \partial u_i/\partial x_j$ (where, u_i, i=1,2,3 are the velocity components) in terms of its symmetric and anti-symmetric parts. We call the symmetric part as the strain-rate tensor, s_{ij}, and the anti-symmetric part as the rotation-rate tensor, Ω_{ij}. Here, we can also write the rotation-rate tensor in terms of vorticity components, ω_k, k=1,2,3 as Ω_{ij} = -(1/2)$\epsilon_{ijk}\omega_k$, where ϵ_{ijk} is the permutation symbol. The characteristic equation of the VGT is

$$\Lambda_i^3 + P\Lambda_i^2 + Q\Lambda_i + R = 0 \tag{1}$$

where Λ_i (i = 1, 2, 3) are the eigenvalues of the VGT. P, Q, R are the first, second, and third invariants of the VGT, respectively. For an incompressible flow, the first invariant of the VGT is zero (P = 0). The second and third invariants of the VGT are given as

$$Q = \frac{1}{4}(\omega_i\omega_i - 2s_{ij}s_{ij}) \tag{2}$$

$$R = -\frac{1}{3}(s_{ij}s_{jk}s_{ki} + \frac{3}{4}\omega_i s_{ij}\omega_j) \tag{3}$$

The discriminant of equation (1) is

$$D = \frac{27}{4}R^2 + Q^3 \tag{4}$$

Having obtained the invariants of the VGT, we can get the invariants of the strain-rate tensor (s_{ij}) by setting ω_i = 0 in equations (2) and (3). Therefore, the invariants of s_{ij} are

$$Q_s = -\frac{1}{2}s_{ij}s_{ij} \tag{5}$$

$$R_s = -\frac{1}{3}s_{ij}s_{jk}s_{ki} \tag{6}$$

Finally, we can get the single invariant of the rotation-rate tensor (Ω_{ij}) by putting $s_{ij} = 0$ in Eq. (2), and it is

$$Q_w = \frac{1}{4}\omega_i\omega_i \tag{7}$$

The main purpose of these invariants is to reveal information regarding the local topology of the flow field. Since the invariants are independent of any coordinate system, these are ideally suited for understanding the internal coherence of the flow.

1. Q,R diagrams

Let us first look at the Q, R diagrams. Note from Eq. (2) that the meaning of the second invariant of VGT is the balance between vorticity and strain-rate magnitudes. Q can have both positive and negative values. This means any flow will have both vorticity- and strain-dominated regions. The Q, R diagrams tell us what is happening to the production terms of the strain and vorticity inside these strain- or vorticity-dominated regions. This can be understood by looking at the mathematical definitions of Q and R. According to Eq. (2), when Q is positive, then the flow is more vortical in nature compared to straining. Conversely, when Q is negative, our flow is dominated by straining motions over rotating motions. Similarly, when we look at Eq. (3), we note that, $R = -\frac{1}{3}s_{ij}s_{jk}s_{ki} - \frac{1}{4}\omega_i s_{ij}\omega_j$, which is nothing but the balance of production of strain versus vorticity as $-s_{ij}s_{jk}s_{ki}$ is positive on average for turbulent flows. This means when $R < 0$ (i.e., $\omega_i s_{ij}\omega_j > -s_{ij}s_{jk}s_{ki}$), on average, the production of vorticity is preferred over the production of strain. We know from classical turbulence theory that the vorticity production ($\omega_i s_{ij}\omega_j$) occurs through strain stretching the vorticity vector and it is called vortex stretching which is believed to cause turbulence cascade. Similarly, when $R > 0$, we have $-s_{ij}s_{jk}s_{ki} > \omega_i s_{ij}\omega_j$ which means that, on average, the

Accepted to Phys. Fluids 10.1063/5.0100334

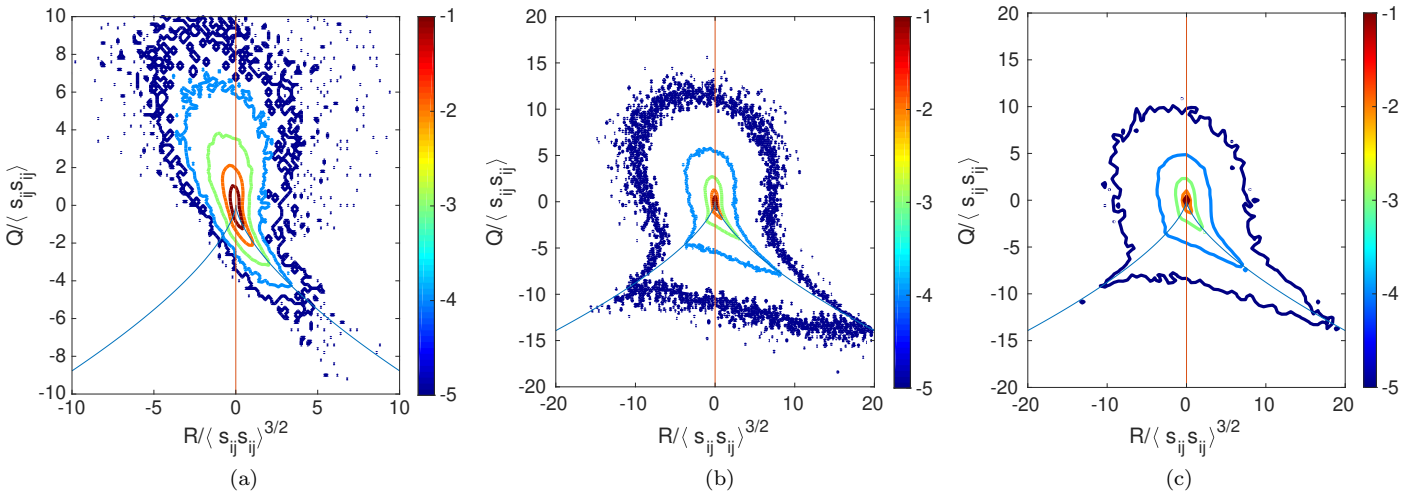

FIG. 1: Joint PDF of Q and R obtained for: (a) HIT, (b) VoF, (c) IBM. The BIT sub-figures are plotted for the US_{-3} station.

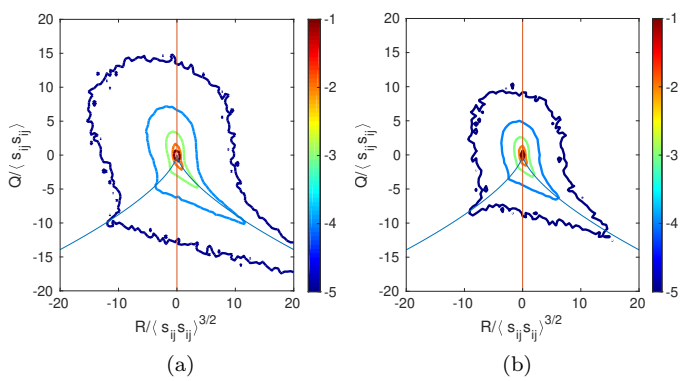

FIG. 2: Joint PDF of Q and R obtained for: (a) VoF (b) IBM at the QS_{-3} station.

flow tends to create more straining over vortical motions.

As we understood the meaning of Q and R, the interpretation of the Q, R diagram becomes much clearer. The Q, R diagram has four quadrants. The upper-left quadrant is where Q is positive and R is negative. This quadrant denotes that there are, on average, vorticity-dominated regions in the flow where the tendency to create vortical motions (vortex stretching) is large than the tendency to create straining motions. This is why this quadrant is marked as Stable-Focus-Stretching (SFS) in the classical literature on VGT kinematics[2,3]. In the upper-right quadrant, $Q > 0$ and $R > 0$, which means that, on average, there are vorticity-dominated regions where the production of strain is dominant over the production of vorticity. This is generally called Unstable-Focus-Compressing (UFC) as the destruction of vorticity happens through the compression of vortical structures by strain. The lower-left quadrant of the $Q - R$ diagram is where, on average, we have strain-dominated flow with the tendency to create more vortical motions as both Q and R are negative in this quadrant. The classical literature calls this quadrant a stable node/saddle/saddle (SN/S/S). Finally, the lower-right quadrant of the $Q - R$ diagram has positive values of R and negative values of Q. Here, on average, we can expect to see a strain-dominated flow with the tendency to produce more straining. This quadrant is commonly known as unstable node/saddle/saddle (UN/S/S).

The typical Q, R diagram of HIT is shown in Fig. 1a. The shape of the JPDF is that of a teardrop and our results agree well with the literature[1–4]. More than 80% of the probability contours in this figure are located in upper-left and lower-right quadrants while the upper-left quadrant alone accounts for more than 50% of probability contours. This shows that the HIT is overall vorticity-dominated turbulence although there are locally strain-dominated regions inside it. Moreover, the Q, R diagram for HIT also reveals to us that, wherever we have vorticity-dominated regions inside the HIT, they have the tendency to produce more vorticity through vortex stretching. On the other hand, the locally strain-dominated regions inside the HIT has more tendency to produce straining motions.

Accepted to Phys. Fluids 10.1063/5.0100334

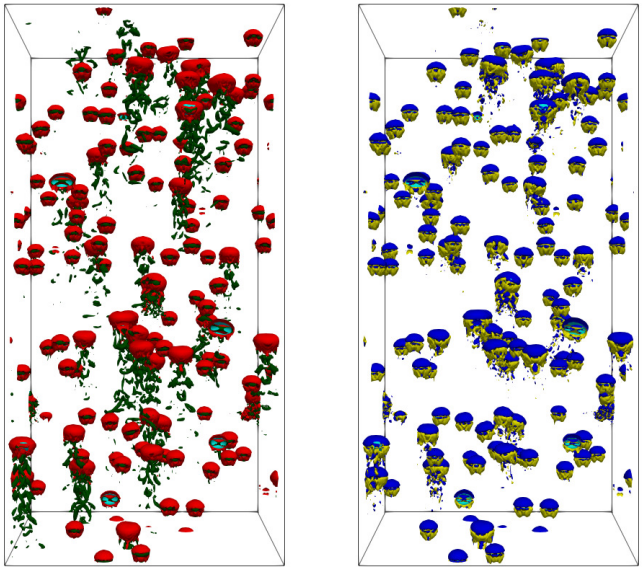

(a) (b)

FIG. 3: (a) Iso-surfaces of positive (green) and negative (red) Q values, (b) Iso-surfaces of positive (blue) and negative (yellow) R values at the US_{-3} station.

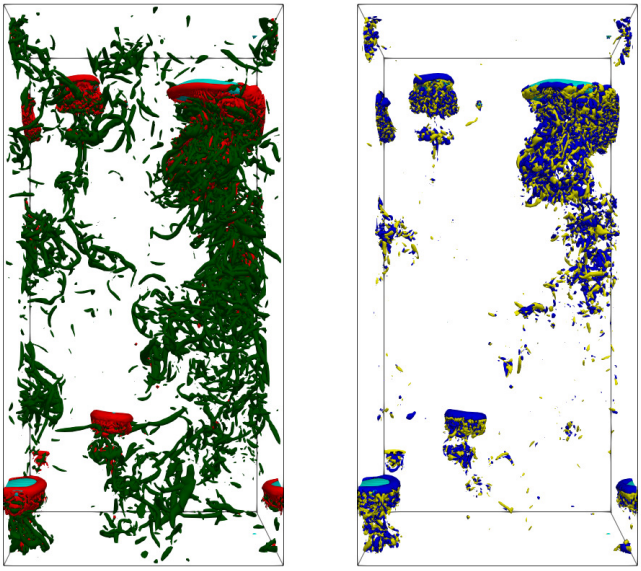

(a) (b)

FIG. 4: (a) Iso-surfaces of positive (green) and negative (red) Q values, (b) Iso-surfaces of positive (blue) and negative (yellow) R values at the QS_{-3} station.

Now, let us consider Q, R diagrams for the continuous phase of BIT. Figs. 1b and 1c present the Q, R diagrams at US_{-3} station obtained from VoF and IBM respectively. We see some remarkable differences in these figures compared with that of HIT. Firstly, the bottom-right and bottom-left quadrants have as much significance as the upper-right and upper-left quadrants. This shows that, on average, the BIT is approximately occupied by both vorticity- and strain-dominated regions. To corroborate this conclusion, Fig. 3a shows that the strain-dominated regions are on the upper and sides of the bubble while the vorticity-dominated regions are in the wake region. Since the time instance of this instantaneous plot is such that the wakes from the bubbles have not yet reached the other bubbles, the top surface of the bubbles generates straining motions besides the side surfaces of the bubble.

Secondly, the lower-left quadrant, which does not have many probability contours in HIT, has some significant amount of probability contours in BIT. This means that vortex stretching is happening even in strain-dominated regions. The implication is that the strain-dominated structures are under the action of destruction as the vortex stretching is a sink term for strain rate. Fig. 3b shows the presence of vortex stretching in the wake region while the production of strain on the top and sides of the bubble. Therefore, the presence of a kink in the lower-left quadrant is the result of strain-dominated structures from the sides of the bubble subject to the action of vortex stretching in the wake.

Finally, and most importantly, we do not observe a clearly-defined preference in the upper-left quadrant of BIT. For a long time, it has been believed that the energy cascade is due to the vortex stretching phenomenon. If vortex stretching is indeed causing the cascade in BIT, then we would have seen a preference for vortex stretching in the upper-right quadrant. Here, however, the shape of the JPDF in positive Q is almost symmetric with respect to the $R = 0$ axis. This makes us conclude that vortex stretching alone cannot be the cause of the energy cascade in BIT.

Now comparing the Q, R diagrams obtained from VoF and IBM, we see that both simulations yield the same results. This can be clearly seen for the QS_{-3} station plotted in Fig. 2. There will be minimal breakup and coalescence in the VoF simulation for the QS_{-3} station where the bubbles undergo deformation. As a result, Fig. 2 shows that the bubble deformation also does not affect the small-scale kinematics of BIT. We still see the kink in the left branch of the $D = 0$ line which is the result of the memory effect as the bubbly flow remembers how the velocity gradients were generated during the initial stages of development. This can be clearly seen in the isocontours of flow structures for the QS_{-3} station plotted in Fig. 4. Since the bubble wakes have fully met at this time instant, the top surface of the bubble no longer serves as the source of the strain-dominated region for QS_{-3} station (see Fig. 4a). Here, as seen in Fig. 4a, the strain-dominated structures are located at the sides of the bubble. At the same time, vortex stretching is also present there. This is the reason we have a clearly defined lower-left quadrant of the $Q - R$ diagram for BIT.

Accepted to Phys. Fluids 10.1063/5.0100334

At the QS_{-3} station also, the JPDFs do not show any significant preference for vortex stretching and the bubbly flows seem to have both strain- and vorticity-dominated regions.

Comparing the results of VoF and IBM for the stations US_{-3} and QS_{-3}, we note that the Q, R diagrams of the IBM simulation look nearly similar in both stations (see figures 1c and 2b). This is because the bubbles do not break up and coalesce in the IBM simulation which results in almost identical statistics once the wakes have started developing. On the other hand, the bubbles break up and coalesce in the VoF simulation which leads to larger bubbles as the flow develops (please see figures 5 and 7 in the first part[31]). This causes a drastic change in statistics of VoF simulation between the stations US_{-3} and QS_{-3}.

To summarize the results from the Q, R diagrams, we note that the BIT comprises both vorticity- and strain-dominated regions. While the strain-dominated regions are subjected to both strain self-amplification and vortex stretching, we do not see any clear preference for vortex stretching in vorticity-dominated regions. Our observations also support the recent developments in turbulence theory that the energy cascade cannot happen solely by vortex stretching.

2. Q_s, R_s diagrams

While the Q, R diagram gives us information about both the straining and vortical regions in the flow, the Q_s, R_s diagram is exclusive for the straining regions in the flow. This can be understood from Eqs. (5) and (6) which represent the invariants of the strain-rate tensor. Here, the strain-rate tensor has three eigenvalues which are represented as λ_i (where i=1,2,3). These strain-rate eigenvalues are ordered as $\lambda_1 > \lambda_2 > \lambda_3$. For incompressible flow, $\lambda_1 + \lambda_2 + \lambda_3$=0. Also, in general, λ_1 >0 and λ_3 <0 while λ_2 can have both positive and negative values. Now, the Q_s, R_s diagram tells us what would be the structure of these straining regions as R_s can be written as $R_s = -\lambda_1\lambda_2\lambda_3$. When R_s is positive, we have two extensive strain-rate eigenvalues (λ_1 and λ_2) and one compressing strain-rate eigenvalue (i.e., λ_3). Therefore, there is more tendency to generate sheet-like structures through which strain is amplified. When R_s is negative, we have two compressing and one extensive strain-rate eigenvalues which lead to tube-like structures.

Besides the geometry of the straining regions, Q_s, R_s diagram also tells us the nature of expansion and contraction of strain-rate eigenvalues since we can write R_s as,

$$R_s = (-Q_s)^{3/2} a(1+a)(1+a+a^2)^{-3/2} \tag{8}$$

where $a = \lambda_1/\lambda_2$. When the ratio of eigenvalues are 2:-1:-1 (a=-1/2), we have tube-like straining structures which are subject to axisymmetric contraction. When sheet-like straining structures are preferred, they can be under (i) axisymmetric expansion (axial stretching) for the strain-rate eigenvalues ratio of 1:1:-2 (a=1), and/or (ii) bi-axial expansion when the ratio is 3:1:-4 (a=1/3). When $a = 0$, the ratio of strain-rate eigenvalues read as 1:0:-1 which represent two-dimensional flow.

The Q_s, R_s diagram for HIT is shown in Fig. 5a. The JPDF is skewed towards positive R_s which shows that the straining regions of HIT are sheet-like and they tend to generate strain through strain self-amplification. The most probable type of expansion in HIT is between axial and biaxial stretching by strain. Now, when we look at the Q_s, R_s diagrams obtained at the US_{-3} station, we note some remarkable differences compared with HIT. In both VoF and IBM, we see that the JPDF is also defined on the negative R_s side. This reveals that the BIT has both sheet- and tube-like straining structures in it while the HIT has more prevalence of sheet-like structures. In BIT, the tube-like structures are generated by axial contraction which is mostly absent in HIT. The presence of tube-like structures also signifies the fact that the amount of strain in these straining regions are progressively destroyed. As in HIT, the sheet-like straining structures of BIT are also due to both axial and bi-axial expansion.

The Q_s, R_s diagram at the station QS_{-3} is shown in Fig. 6. We see from this figure that the bubble deformation does not influence the small-scale kinematics. Here also, we see the presence of tube-like structures in the straining regions of BIT in both VoF and IBM albeit the probability of finding such structures is greatly reduced from the station US_{-3}. As in the station US_{-3}, at this station also the tube-like structures are due to axial contraction, and the sheet-like structures are due to both axial and bi-axial expansion. As with the Q, R diagrams, the Q_s, R_s diagrams of the IBM simulations also remain nearly the same from the US_{-3} to QS_{-3} stations. Therefore, the explanation rendered for the Q, R diagrams in the previous section is also applicable here.

To summarize, the Q_s, R_s diagram of BIT is different from the HIT as the BIT has both tube- and sheet-like straining structures present in unsteady and quasi-steady states. The presence of tube-like straining structures aid in the destruction of strain in BIT which is peculiar to these flows. Just like Q, R diagrams, Q_s, R_s diagrams are also not influenced by the deformation, breakup and coalescence of bubbles as both VoF and IBM yield similar Q_s, R_s diagrams.

3. $-Q_s, Q_w$ diagrams

The final JPDF in analysing VGT is the $-Q_s, Q_w$ diagrams. They help us to study the geometry of turbulent kinetic energy dissipation. To understand this better, we know that the dissipation of turbulent kinetic energy is given as $\epsilon = 2\nu < s_{ij}s_{ij} >$, where the angular brackets represent appropriate averaging. Also, we know for HIT that $\omega_i\omega_i = 2 < s_{ij}s_{ij} >$ (see Table I). Therefore, dissipa-

Accepted to Phys. Fluids 10.1063/5.0100334

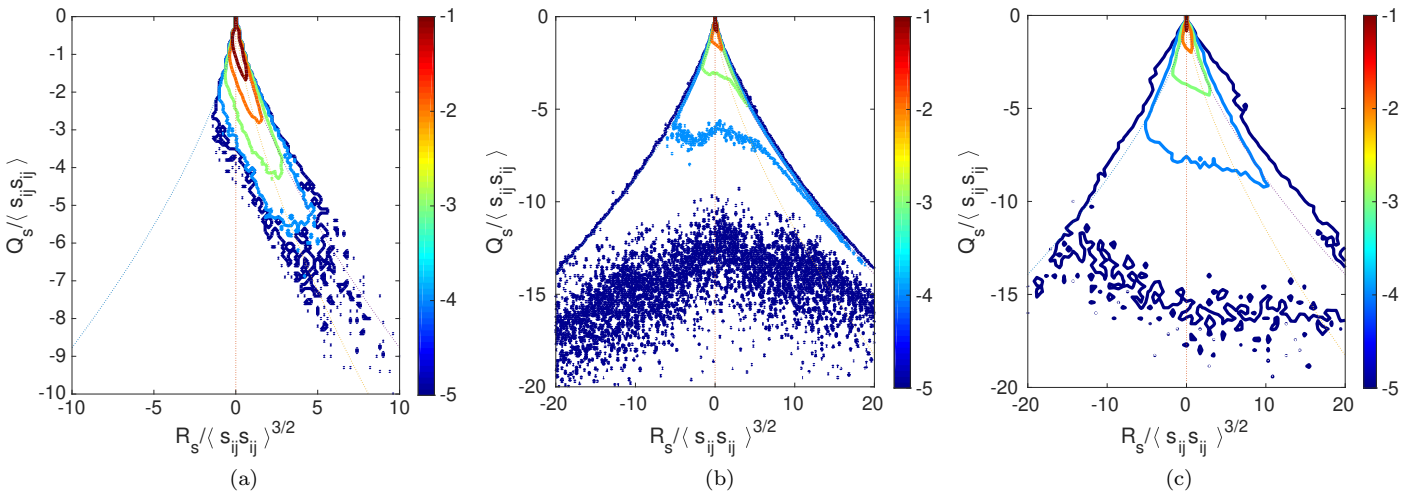

FIG. 5: Joint PDF of Q_s and R_s obtained for: (a) HIT, (b) VoF, (c) IBM. The BIT sub-figures are plotted for the US_{-3} station. The four dotted lines from the left to the right in these sub-figures represent the strain-rate eigenvalues ratio λ_1:λ_2:λ_3 = 2:-1:-1, 1:0:-1, 3:1:-4 and 1:1:-2.

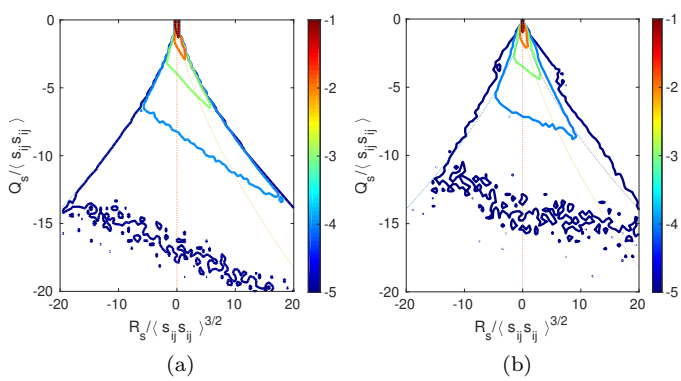

FIG. 6: Joint PDF of Q_s and R_s obtained for: (a) VoF (b) IBM at the QS_{-3} station. The four dotted lines from the left to the right in these sub-figures represent the strain-rate eigenvalues ratio λ_1:λ_2:λ_3 = 2:-1:-1, 1:0:-1, 3:1:-4 and 1:1:-2.

Simulation	$< \omega_i\omega_i > / < s_{ij}s_{ij} >$
HIT	2.0
BIT/VoF: US_{-3}	1.75
BIT/IBM: US_{-3}	1.91
BIT/VoF: QS_{-3}	1.8
BIT/IBM: QS_{-3}	1.95

TABLE I: Values of $< \omega_i\omega_i > / < s_{ij}s_{ij} >$ for BIT and HIT

tion can be written in terms of both strain and vorticity. In the $-Q_s, Q_w$ diagram, we consider -Q_s on the y-axis and Q_w on the horizontal axis. Therefore, both axes are always positive. When the JPDF falls on the horizontal line, this means that the dissipative structures are mostly made up of vortex tubes. On the other hand, when the JPDF is along the vertical axis, this signifies that the dissipating structures are of irrotational strain. A 45° line on this JPDF represents the equal probability for enstropy and strain and this is marked by vortex sheets.

The $-Q_s, Q_w$ diagram of HIT is shown in Fig. 7a. Here, every self-similar JPDF contour has a maximum of Q_w, which is almost twice that of -Q_s revealing an equal probability for sheet- and tube-like dissipative structures with the intensity of enstrophy is, on average, higher than strain. This shows that HIT is a vorticity-dominated flow. Further proof to this can be seen in Table I, that shows that the magnitude of $< \omega_i\omega_i >$ is twice that of $< s_{ij}s_{ij} >$. Fig. 7b shows that $-Q_s, Q_w$ diagram for BIT at the station US_{-3} obtained using VoF. Once again, we note some marked differences compared with the HIT result. Here, the JPDF is aligned towards the y-axis signifying that the dissipative structures are highly

Accepted to Phys. Fluids 10.1063/5.0100334

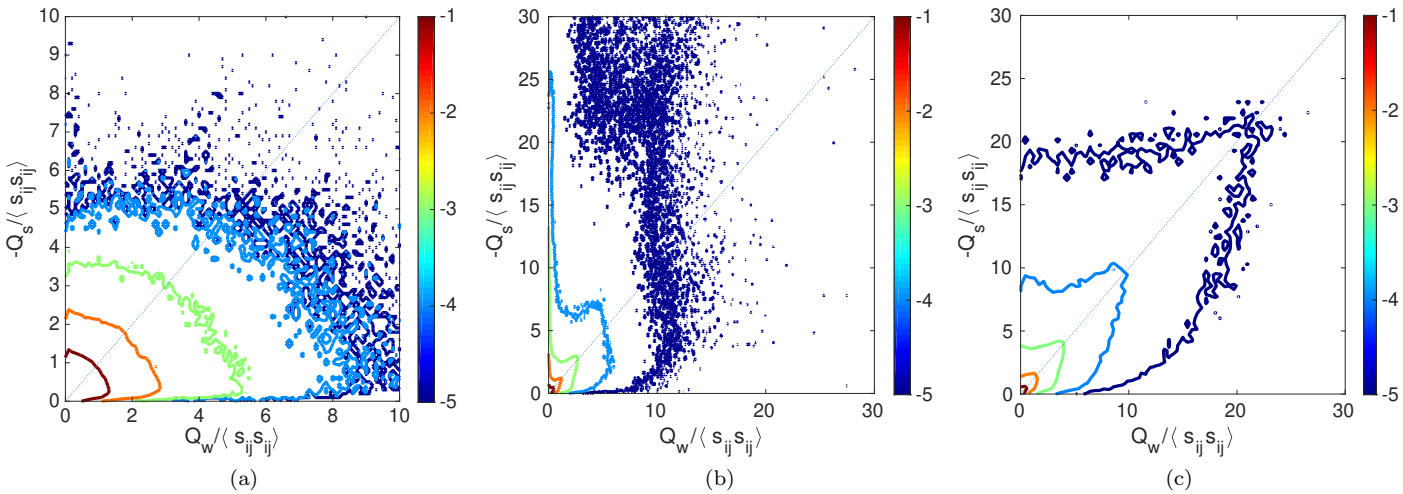

FIG. 7: Joint PDF of $-Q_s$ and Q_w obtained for: (a) HIT, (b) VoF, (c) IBM. The BIT sub-figures are plotted for the US_{-3} station.

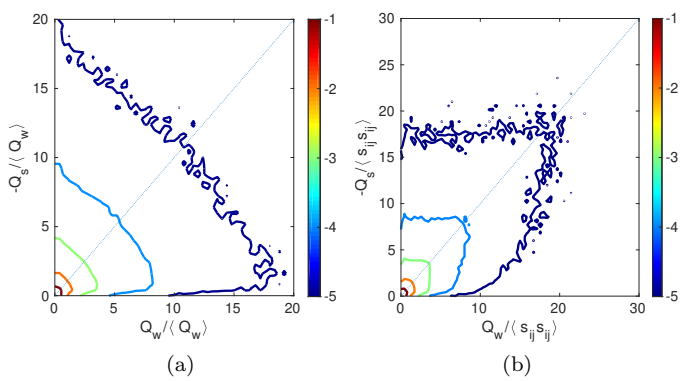

FIG. 8: Joint PDF of $-Q_s$ and Q_w obtained for: (a) VoF (b) IBM at the QS_{-3} station.

irrotational and the BIT at this station is highly strain-dominated. This can also be seen from the Table I that the ratio of $< \omega_i\omega_i >/< s_{ij}s_{ij} >$ is no longer two but it is 1.75. This value also tells us that the BIT is anisotropic even at small scales. When we look at the $-Q_s, Q_w$ diagram obtained from IBM at the US_{-3} station, we note some differences compared to the BIT result of VoF. Here, the dissipative structures are made of sheet-like structures on average with the intensity of strain being only slightly larger than the enstropy. This is also reflected in the value of $< \omega_i\omega_i >/< s_{ij}s_{ij} >$ obtained for this station using IBM as shown in Table I.

As the flow develops, Fig. 8a tells us that the dissipative structures in BIT with coalescence and breakup transform from irrotational to equal probability for both sheet- and tube-like structures. Yet, the magnitude of enstropy is not higher than strain as in the case of HIT. Rather we see a slightly higher magnitude for strain over enstropy for every self-similar JPDF contour. This shows that the BIT with coalescence and breakup remain anisotropic at all times. This is further reflected in Table I as the ratio $< \omega_i\omega_i >/< s_{ij}s_{ij} >$ is still not 2. In the case of BIT without breakup and coalescence, however, the dissipative structures remain sheet-like for all times as we do not see many differences between Figs. 7c and 8b. In this case, also, the BIT remains anisotropic even at the small scales (see Table I). As we noted and explained for the Q, R diagrams, here also the statistics of IBM simulation only vary marginally from the US_{-3} to QS_{-3} stations.

In summary, the BIT with and without breakup and coalescence exhibit some differences at small scales when considering $-Q_s, Q_w$ diagrams. On one hand, the BIT with breakup and coalescence evolve from purely irrotational dissipative structures to equal probability for both sheet- and tube-like dissipative structures. On the other hand, the dissipative structures in the BIT without breakup and coalescence remain sheet-like at all times. Yet, both cases are strain-dominated anisotropic turbulence even at small scales.

Accepted to Phys. Fluids 10.1063/5.0100334

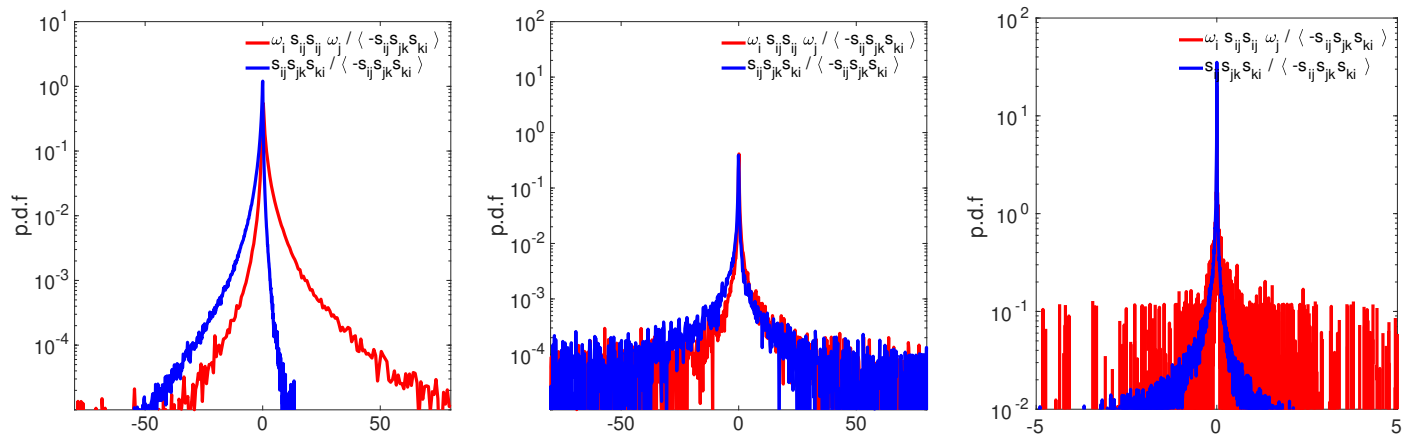

(a) (b) (c)

FIG. 9: PDFs of production terms of vorticity (red) and strain (blue) obtained for: (a) HIT, (b) VoF, (c) IBM. The BIT sub-figures are plotted for the US_{-3} station.

B. Production terms of fine-scale turbulence

Having looked at the JPDF of various invariants related to VGT, strain-rate and rotation-rate tensor, this section further explores the source terms of VGT. We noted during the discussion of VGT that the building blocks of invariants of VGT are vorticity (ω_i) and strain (s_{ij}). These quantities are also governed by the following equations:

$$\frac{\partial \frac{1}{2}\omega_i\omega_i}{\partial t} + u_j \frac{\partial \frac{1}{2}\omega_i\omega_i}{\partial x_j} = \omega_i s_{ij} \omega_j + \nu \omega_i \frac{\partial^2 \omega_i}{\partial x_j \partial x_j} \tag{9}$$

$$\begin{aligned} \frac{\partial \frac{1}{2} s_{ij} s_{ij}}{\partial t} + u_j \frac{\partial \frac{1}{2} s_{ij} s_{ij}}{\partial x_j} &= -s_{ij} s_{jk} s_{ki} - \frac{1}{4}\omega_i s_{ij} \omega_j \\ &- s_{ij} \frac{\partial p}{\partial x_i \partial x_j} + \nu s_{ij} \frac{\partial^2 s_{ij}}{\partial x_j \partial x_j} \end{aligned} \tag{10}$$

As can be seen from these equations, the kinematics of vorticity and strain are intertwined. Strain appears in the production term of enstropy as $\omega_i s_{ij} \omega_j$. As we saw earlier, this term is called vortex stretching. Interestingly, the same term acts as a sink for strain (see Eq. (10)) acting as a depleting mechanism for strain. The production of strain occurs through a mechanism called strain self-amplification which is represented by the term $s_{ij} s_{jk} s_{ki}$. Therefore, to understand further about the kinematics of small-scale turbulence, we need to explore these source terms further. These source terms can be written as,

$$\begin{aligned} \omega_i s_{ij} \omega_j = \omega^2 \lambda_1 cos^2(\boldsymbol{\omega}, \boldsymbol{e_1}) + \omega^2 \lambda_2 cos^2(\boldsymbol{\omega}, \boldsymbol{e_2}) + \\ \omega^2 \lambda_3 cos^2(\boldsymbol{\omega}, \boldsymbol{e_3}) \end{aligned} \tag{11}$$

$$s_{ij} s_{jk} s_{ki} = \lambda_1^3 + \lambda_2^3 + \lambda_3^3 \tag{12}$$

where $\omega^2 = \omega_i \omega_i$, $\boldsymbol{\omega}$ is the vorticity vector and $\boldsymbol{e_i}$ (i=1,2,3) are the eigenvectors of the strain-rate tensor.

These equations reveal that the strain self-amplification depends on strain-rate eigenvalues while the vortex stretching term depends on strain-rate eigenvalues and the alignment between vorticity vector and strain-rate eigenvectors. Therefore, in this subsection, we first look at the PDFs of these production terms and then analyse the strain-rate eigenvalues and eigenvectors and their alignment with the vorticity vector.

1. Vortex stretching and strain self-amplification

We analyse the production terms of strain and vorticity in this subsection. The PDFs of vortex stretching and strain self-amplification terms for HIT are shown in Fig. 9a. The PDF of $\omega_i s_{ij} \omega_j$ is skewed to the positive which means that, on average, vortex stretching is preferred over compression in HIT. The PDF of $s_{ij} s_{jk} s_{ki}$ is skewed to negative with very few positive values. Since the source term of strain production is -$s_{ij} s_{jk} s_{ki}$, the PDF clearly shows that the production of strain is more preferred than its destruction. The rela-

Accepted to Phys. Fluids 10.1063/5.0100334

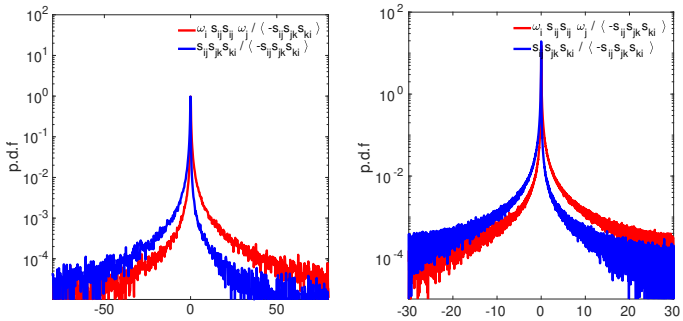

(a) (b)

FIG. 10: PDFs of production terms of vorticity (red) and strain (blue) obtained for: (a) VoF, (b) IBM at the QS_{-3} station.

Simulation	$< \omega_i s_{ij} \omega_j > / < s_{ij} s_{jk} s_{ki} >$
HIT	1.33
BIT/VoF: US_{-3}	1.05
BIT/IBM: US_{-3}	1.04
BIT/VoF: QS_{-3}	0.99
BIT/IBM: QS_{-3}	1.01

TABLE II: Values of $< \omega_i \omega_i > / < s_{ij} s_{ij} >$ for BIT and HIT

tive strength between the enstropy production and strain self-amplification is reported for HIT in Table II. We see from this table that, on average, the strength of enstropy production is larger than that of strain. This is typical of HIT as it is a vorticity-dominated flow[1–4].

The PDFs of $\omega_i s_{ij} \omega_j$ and $s_{ij} s_{jk} s_{ki}$ at the US_{-3} station is plotted for BIT with breakup and coalescence and for without breakup and coalescence in Figs. 9b and 9c respectively. The wider tails in these PDFs show the presence of intense and intermittent events. Although the PDF of strain self-amplification is only slightly skewed to the negative, we still see some rare yet intense strain destruction events. These events are visible in the results obtained when the BIT is with breakup and coalescence (Fig. 9b). The PDF of $\omega_i s_{ij} \omega_j$ is also only slightly skewed to positive and here also the presence of rare intense vortex compression events can be seen. The effect of these rare events is that they decrease the strength of vorticity and strain in this station. Looking at the ratio between these two production terms in Table II, we see that the ratio is almost one. We know from the Q, R diagrams at this station that the vortex stretching is weak. Now, we also learn that the strength of the strain self-amplification process is weak too. This is the

Simulation	$\frac{<\lambda_1^3>}{<s_{ij}s_{jk}s_{ki}>}$	$\frac{<\lambda_2^3>}{<s_{ij}s_{jk}s_{ki}>}$	$\frac{<\lambda_3^3>}{<s_{ij}s_{jk}s_{ki}>}$
HIT	0.92	0.06	-2.03
BIT/VoF: US_{-3}	10.30	0.16	-11.49
BIT/IBM: US_{-3}	9.23	0.11	-10.76
BIT/VoF: QS_{-3}	2.24	0.06	-3.29
BIT/IBM: QS_{-3}	2.11	0.06	-2.45

TABLE III: Values of $< \omega_i \omega_i > / < s_{ij} s_{ij} >$ for BIT and HIT

reason why the ratio is close to one. In connection to the energy cascade at this station, we note that the -3 slope is clearly defined in the region where neither the vortex stretching nor the strain self-amplification is strong. It is generally believed in classic turbulence literature that the vortex stretching is the one causing the -5/3 slope in the energy spectrum of homogeneous isotropic turbulence[32]. Recent research works, however, continue to shed light that it is not only vortex stretching but also the strain self-amplification that matter to the appearance of the -5/3 slope[33,34]. We report a peculiar -3 slope in the energy spectrum where there is neither vortex stretching nor strain self-amplification is strong.

As we move to the station QS_{-3}, we start to see the PDFs of $\omega_i s_{ij} \omega_j$ and $s_{ij} s_{jk} s_{ki}$ becoming skewed to the positive and negative respectively. Yet, as in the station US_{-3}, here also the rare intense events continue to exist and this could answer why the ratio of $< \omega_i s_{ij} \omega_j >/< s_{ij} s_{jk} s_{ki} >$ is close to one at this station.

2. Eigenvalues of strain-rate tensor

Having looked at the behaviour of vortex stretching and strain self-amplification, this subsection answers why such a behaviour is noted in BIT. To understand strain self-amplification, we need to look at the strain-rate eigenvalues as per Eq. (12).

The PDFs of strain-rate eigenvalues are shown in Fig. 11a for HIT. The figure shows that the extensive eigenvalue λ_1 is always positive and the compressive eigenvalue (λ_3) is always negative. The intermediate eigenvalue (λ_2) can have both positive and negative and for HIT, the PDF of the intermediate strain-rate eigenvalue is skewed to the right. Since $-s_{ij} s_{jk} s_{ki} = -(\lambda_1^3 + \lambda_2^3 + \lambda_3^3)$. The positivity of $-s_{ij} s_{jk} s_{ki}$ should be coming from λ_3 whose PDF is strongly skewed to the negative for HIT giving rise to a strong strain of self-amplification. As we see in the next subsection, λ_1 and λ_3 determine the strength of vortex stretching. For HIT, the intermediate strain-rate eigenvalue is strongly skewed to the positive giving rise to stronger vortex stretching. The averaged values

Accepted to Phys. Fluids 10.1063/5.0100334

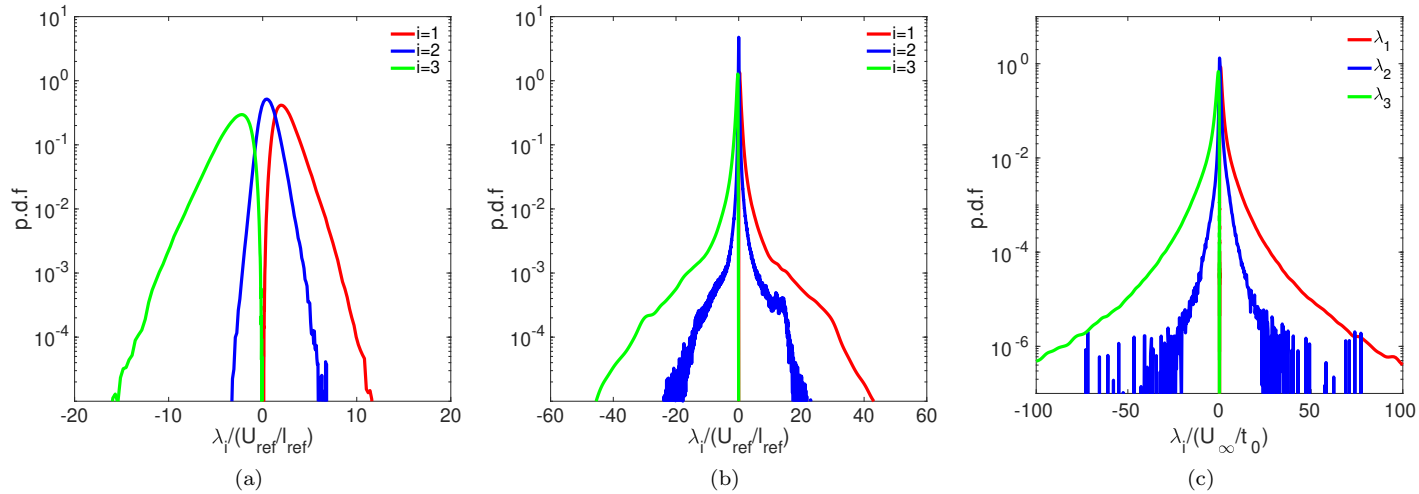

FIG. 11: PDFs of strain-rate eigenvalues obtained for: (a) HIT, (b) VoF, (c) IBM. The BIT sub-figures are plotted for the US_{-3} station.

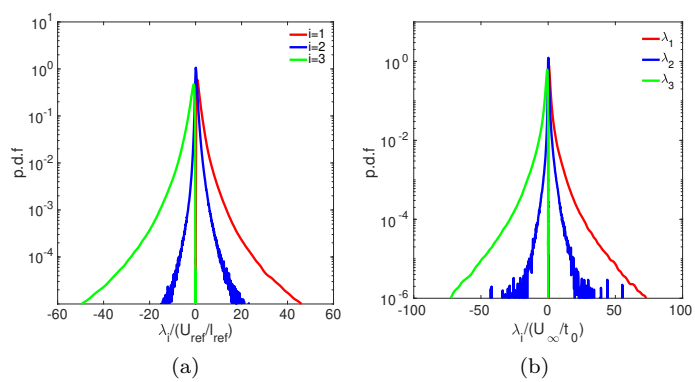

FIG. 12: PDFs of strain-rate eigenvalues obtained for: (a) VoF, (b) IBM at the QS_{-3} station.

of strain-rate eigenvalues are tabulated for HIT in Table III. On average, we have two positive and one negative strain-rate eigenvalues which resemble a sheet-like structure for strain self-amplification. The averaged value of λ_3 is much larger than the values of λ_1 and λ_2 reinforcing the previous observation that HIT has a strong strain self-amplification mechanism.

The PDF of strain-rate eigenvalues for BIT using VoF and IBM at the station US_{-3} is plotted in Fig. 11b and 11c. The first thing to note is that the intermediate strain-rate eigenvalue is weakly skewed to the positive and this explains why the vortex stretching is weak at this station for BIT with and without breakup and coalescence. The PDFs as well as the mean values of λ_1 and λ_3 show that the magnitude of these strain-rate eigenvalues is similar while for HIT the magnitude of $< \lambda_3 >$ is much higher than $< \lambda_1 >$. As discussed in the previous paragraph, the weak magnitude of $< \lambda_3 >$ compared with $< \lambda_1 >$ leads to a weak strain self-amplification mechanism at this station in both VoF and IBM simulations.

Moving to the station QS_{-3}, we observe in Fig. 12 that the PDF of the intermediate strain-rate eigenvalue is skewed to the positive which would lead to a stronger vortex stretching compared to the station US_{-3}. Yet, Fig. 12 and Table III reveal that the absolute magnitude of λ_3 continues to be close to λ_1 both in the PDF and when time-averaged. This shows that the mechanism of strain self-amplification is weaker at all times in BIT with and without breakup and coalescence.

In a summary, we see that the vortex stretching is weak at the station US_{-3} but it improves in the station QS_{-3}. The strain self-amplification, however, remains weak at all times. These results are in contrast to HIT where stronger vortex stretching and strain self-amplification is reported.

3. Alignment between vorticity vector and strain-rate eigenvectors

Finally, this subsection looks at the geometric alignments between the vorticity vector and strain-rate eigen-

Accepted to Phys. Fluids 10.1063/5.0100334

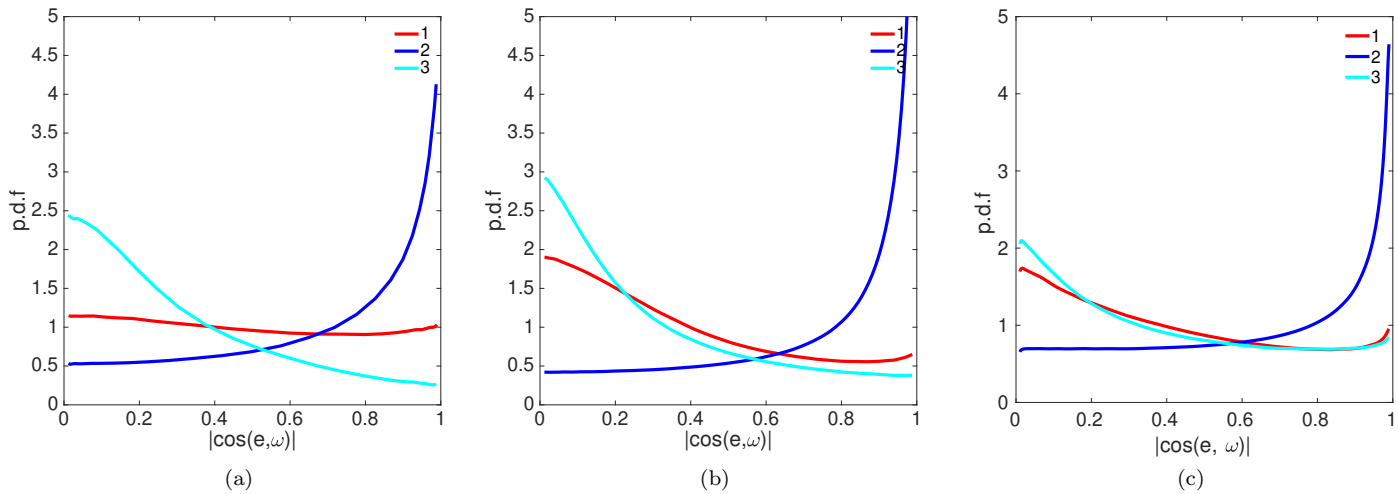

FIG. 13: PDFs of the alignment between vorticity vector and strain-rate eigenvectors obtained for: (a) HIT, (b) VoF, (c) IBM. The BIT sub-figures are plotted for the US_{-3} station. Two vectors aligning randomly with each other will have a horizontal straight line across the abscissa.

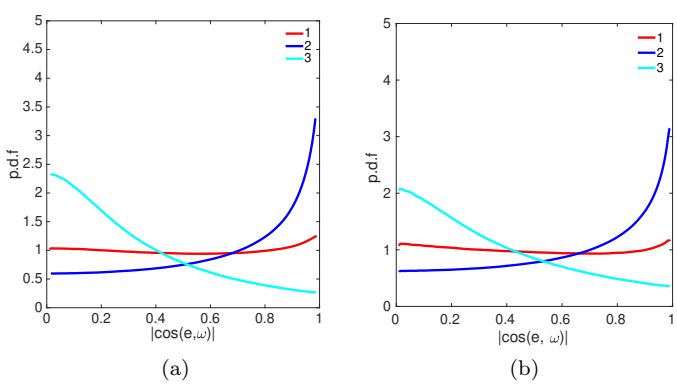

FIG. 14: PDFs of the alignment between vorticity vector and strain-rate eigenvectors obtained for: (a) VoF, (b) IBM at the QS_{-3} station.

vectors as Eq. (11) tells us that the vortex stretching term also depends on these alignments besides the strain-rate eigenvalues. Since the production of enstrophy occurs through vortex stretching, one might expect to see the vorticity vector aligning with the extensive strain-rate eigenvector. The literature on HIT, however, shows that the vorticity vector aligns strongly with the intermediate strain-rate eigenvector and aligns weakly with the extensive strain-rate eigenvector as seen in Fig. 13a. Since the intermediate strain-rate eigenvalue is skewed to the positive for HIT, the strong alignment of its eigenvector with the vorticity vector results in strong vortex stretching.

For BIT with and without breakup and coalescence at the station US_{-3}, we note that the intermediate strain-rate eigenvector aligns with the vorticity vector but the extensive strain-rate eigenvector aligns perpendicular to the vorticity vector in both VoF and IBM simulations (Figs. 13b and 13c). As a result, we now have a better idea as to why the vortex stretching is weak for BIT at the station US_{-3}. On one hand, we have the intense extensive eigenvalues whose eigenvector aligns perpendicular to the vorticity vector and thus making void of these intense eigenvalues. On the other hand, although the intermediate strain-rate eigenvector is strongly aligned with the vorticity vector, its eigenvalue is only slightly skewed to the positive and thus does not lead the strong alignment towards a meaningful vortex stretching.

Now, we need to answer why the geometrical alignments are not universal at the station US_{-3}. An answer to this question can be obtained from the literature in multiscale turbulence which reports a different geometrical alignment to this study as well as to HIT[5]. There, the strain near the multi-scale grid was due to the action of pressure Hessian and thus the properties of such a strain are very different to the one generated by strain self-amplification and this leads to a different geometrical alignment. The same explanation can be extrapolated to the station US_{-3} too. We know that the strain self-amplification mechanism is very weak at this location.

Accepted to Phys. Fluids 10.1063/5.0100334

We also know from part one of this study that the flow at this station is dominated by pressure Hessian. Therefore, the strain field at this station is not the classical strain field. Rather, it is dominated by irrotational strain due to pressure Hessian. Due to this, the nature of vorticity alignment with this unusual strain field differs from the classical results.

Moving to the station QS_{-3}, the geometrical alignments start to appear to be universal with the intermediate strain-rate eigenvector aligning strongly with the vorticity vector and the extensive strain-rate eigenvector aligning weakly with the vorticity vector (see Fig. 14). This behaviour would result in stronger vortex stretching. The compressing eigenvector aligns perpendicular to the vorticity vector.

To summarize the result of the geometrical alignments, the BIT with and without breakup and coalescence exhibits a very different geometrical alignment to that of HIT where only the intermediate strain-rate eigenvector aligns strongly with the vorticity vector and thus paving way for a weak vortex stretching. At the station QS_{-3}, however, the geometrical alignments of BIT translate to that of HIT. It appears that the strain at the station US_{-3} is not the classical strain field that is generated due to the strain itself. This leads to a different geometrical alignment. Interestingly, the bubble topology, deformation, breakup and coalescence do not influence the geometrical alignments at small scales.

IV. SUMMARY AND CONCLUSIONS

We studied bubble induced turbulence of dilute bubbly flows using direct numerical simulations. The objectives of this study are two-fold. First, we sought to establish the role of bubble deformation, breakup and coalescence on the fine-scale kinematics of BIT. For this reason, we simulated the bubbly flows using two distinct numerical methods. In the volume of fluid method, the bubbles were allowed to break up and coalesce. On the other hand, the immersed boundary method treated bubbles as rigid spheres and thus no bubble breakup and coalescence processes are allowed. We compared the kinematic small-scale BIT results of these two simulations to establish how much the bubble deformation, breakup and coalescence influence the fine-scale kinematics. In the second objective, we wanted to understand whether the universal fine-scale characteristics reported for the classical homogeneous isotropic turbulence can also be seen in BIT. To this end, we took the seven notable universal fine-scale HIT characteristics and observed the same in our HIT simulation also. Then to establish whether fine-scale BIT also exhibits these characteristics we compared the results of HIT with that of BIT.

The first important takeaway from this study is that the bubble deformation, breakup and coalescence play little to no role in setting up the kinematics of fine-scale turbulence. Both the VoF and IBM simulations yield similar results on most aspects of the fine-scale turbulence. The only difference between the VoF and IBM simulations is noted in terms of dissipating structures. While the structure of dissipation remains sheet-like throughout the simulation for IBM, they change from being irrotational to equal probability for sheet- and tube-like structures in VoF. Apart from this difference, every other characteristic of fine-scale BIT is the same for both VoF and IBM simulations.

We found significant differences between HIT and BIT in terms of fine-scale kinematics. While the Q-R diagram of the HIT is in the shape of a teardrop (which resembles that the vortex stretching is preferred over vortex compression in the vorticity-dominated region and the strain self-amplification is preferred over strain self-destruction in the strain-dominating region), such behaviour is not noted for BIT. Here, there is a significant portion of the Q, R diagram with the combination of strain dominance and preference for enstrophy production over strain production. We observed that the top and sides of the bubbles give rise to such an intriguing aspect of highly straining elements undergoing predominant vortex stretching. Consequently, the strain-dominated region in BIT is not only sheet-like, as in the case of HIT, but they are also tube-like. This behaviour is more profound in the VoF simulation as noted in the Q_s, R_s diagrams. It was also noted that the BIT is anisotropic even at small scales as the magnitude of averaged enstrophy is found to be less than twice the average strain-squared. The next important difference is the vortex stretching term which is found to be very weak in BIT. The reason for this weak vortex stretching is found to be two-fold. First, the intermediate strain-rate eigenvalue is weakly skewed to the positive. Second, although the extensive strain-rate eigenvalue is strongly skewed to the positive, its eigenvector aligns perpendicular to the vorticity vectors rendering the strong positive values of strain-rate eigenvalues meaningless. For these two reasons, we found a weak vortex stretching mechanism in BIT. It is interesting that, despite this weak vortex stretching mechanism, we still observed a clearly defined -3 slope in the energy spectrum. Adding to the enstrophy production mechanism, we found the mechanism of strain production also to be weak in BIT. This is evident from the fact that time-averaged values of extensive and compressive eigenvalues are almost similar giving rise to a weak strain producing mechanism. Thus, we have found that the kinematics of fine-scale BIT are radically different to that of HIT. We hope that our results would be of paramount importance for developing structure-based large eddy simulation models for the BIT. Although the conclusions made in this research are from a low void-fraction bubbly system, there is a recent study by Mukherjee *et al.*[35] which presents similar results even for a bubbly system of 45% void fraction. Therefore, our results could be universal for any bubbly flows although further studies are needed to prove or disprove this.

Accepted to Phys. Fluids 10.1063/5.0100334

[1] A. E. Perry and M. S. Chong, "A description of eddying motions and flow patterns using critical-point concepts," Annu. Rev. Fluid Mech. **19**, 125–155 (1987).

[2] M. S. Chong, A. E. Perry, and B. J. Cantwell, "A general classification of three-dimensional flow fields," Phys. Fluids **2**, 765–777 (1990).

[3] A. Ooi, J. Martin, J. Soria, and M. S. Chong, "A study of the evolution and characteristics of the invariants of the velocity-gradient tensor in isotropic turbulence," J. Fluid Mech. **381**, 141–174 (1999).

[4] H. M. Blackburn, N. N. Mansour, and B. J. Cantwell, "Topology of fine-scale motions in turbulent channel flow," J. Fluid Mech. **310**, 269–292 (1996).

[5] I. Paul, G. Papadakis, and J. Vassilicos, "Genesis and evolution of velocity gradients in near-field spatially developing turbulence," J. Fluid Mech. **815**, 295–332 (2017).

[6] J. Soria, R. Sondergaard, B. Cantwell, M. Chong, and A. Perry, "A study of the fine-scale motions of incompressible time-developing mixing layers," Phys. Fluids **6**, 871–884 (1994).

[7] R. Zenit, D. L. Koch, and A. S. Sangani, "Measurements of the average properties of a suspension of bubbles rising in a vertical channel," J. Fluid Mech. **429**, 307–342 (2001).

[8] F. Risso and K. Ellingsen, "Velocity fluctuations in a homogeneous dilute dispersion of high-Reynolds-number rising bubbles," J. Fluid Mech. **453**, 395–410 (2002).

[9] J. Martínez-Mercado, C. A. Palacios-Morales, and R. Zenit, "Measurement of pseudoturbulence intensity in monodispersed bubbly liquids for 10<Re< 500," Phys. Fluids **19**, 103302 (2007).

[10] G. Riboux, F. Risso, and D. Legendre, "Experimental characterization of the agitation generated by bubbles rising at high Reynolds number," J. Fluid Mech. **643**, 509–539 (2010).

[11] S. Mendez-Diaz, J. Serrano-Garcia, R. Zenit, and J. Hernandez-Cordero, "Power spectral distributions of pseudo-turbulent bubbly flows," Phys. Fluids **25**, 043303 (2013).

[12] V. N. Prakash, J. M. Mercado, L. van Wijngaarden, E. Mancilla, Y. Tagawa, D. Lohse, and C. Sun, "Energy spectra in turbulent bubbly flows," J. Fluid Mech. **791**, 174–190 (2016).

[13] E. Alméras, V. Mathai, D. Lohse, and C. Sun, "Experimental investigation of the turbulence induced by a bubble swarm rising within incident turbulence," J. Fluid Mech. **825**, 1091–1112 (2017).

[14] J. H. Lee, H. Kim, J. Lee, and H. Park, "Scale-wise analysis of upward turbulent bubbly flows: An experimental study," Phys. Fluids **33**, 053316 (2021).

[15] B. Bunner and G. Tryggvason, "Dynamics of homogeneous bubbly flows part 1. rise velocity and microstructure of the bubbles," J. Fluid Mech. **466**, 17–52 (2002).

[16] J. Lu and G. Tryggvason, "Numerical study of turbulent bubbly downflows in a vertical channel," Phys. Fluids **18**, 103302 (2006).

[17] I. Roghair, J. M. Mercado, M. V. S. Annaland, H. Kuipers, C. Sun, and D. Lohse, "Energy spectra and bubble velocity distributions in pseudo-turbulence: Numerical simulations vs. experiments," Int. J. Multiph. Flow **37**, 1093–1098 (2011).

[18] S. Dabiri, J. Lu, and G. Tryggvason, "Transition between regimes of a vertical channel bubbly upflow due to bubble deformability," Phys. Fluids **25**, 102110 (2013).

[19] J. Lu and G. Tryggvason, "Dynamics of nearly spherical bubbles in a turbulent channel upflow," J. Fluid Mech. **732**, 166–189 (2013).

[20] C. Santarelli and J. Fröhlich, "Direct numerical simulations of spherical bubbles in vertical turbulent channel flow," Int. J. Multiph. Flow **75**, 174–193 (2015).

[21] J. Rensen, S. Luther, and D. Lohse, "The effect of bubbles on developed turbulence," J. Fluid Mech. **538**, 153–187 (2005).

[22] V. Mathai, S. Huisman, C. Sun, D. Lohse, and M. Bourgoin, "Dispersion of air bubbles in isotropic turbulence," Phys. Rev. Lett. **121**, 054501 (2018).

[23] F. Ravelet, C. Colin, and F. Risso, "On the dynamics and breakup of a bubble rising in a turbulent flow," Phys. Fluids **23**, 103301 (2011).

[24] J. Hasslberger, M. Klein, and N. Chakraborty, "Flow topologies in bubble-induced turbulence: a direct numerical simulation analysis," J. Fluid Mech. **857**, 270–290 (2018).

[25] M. S. Dodd and L. Jofre, "Small-scale flow topologies in decaying isotropic turbulence laden with finite-size droplets," Phys. Rev. Fluids **4**, 064303 (2019).

[26] X. Chu, Y. Liu, W. Wang, G. Yang, B. Weigand, and H. Nemati, "Turbulence, pseudo-turbulence, and local flow topology in dispersed bubbly flow," Phys. Fluids **32**, 083310 (2020).

[27] J. Hasslberger, P. Cifani, N. Chakraborty, and M. Klein, "A direct numerical simulation analysis of coherent structures in bubble-laden channel flows," J. Fluid Mech. **905** (2020).

[28] R. Boukharfane, A. Er-Raiy, M. Parsani, and N. Chakraborty, "Structure and dynamics of small-scale turbulence in vaporizing two-phase flows," Scientific reports **11**, 1–21 (2021).

[29] G. Soligo, A. Roccon, and A. Soldati, "Effect of surfactant-laden droplets on turbulent flow topology," Physical Review Fluids **5**, 073606 (2020).

[30] F. Dabbagh and S. Schneiderbauer, "Small-scale flow topologies, pseudo-turbulence, and impact on filtered drag models in turbulent fluidization," Physical Review Fluids **6**, 074301 (2021).

[31] I. Paul, F. Bruno, M. Dodd, and C. Lai, "The role of breakup and coalescence in fine-scale bubble-induced turbulence: part i - dynamics," Phys. Fluids , accepted for publication (2022).

[32] A. Tsinober, *An informal conceptual introduction to turbulence*, Vol. 483 (Springer, 2009).

[33] M. Carbone and A. Bragg, "Is vortex stretching the main cause of the turbulent energy cascade?" J. Fluid Mech. **883** (2020).

[34] P. Johnson, "Energy transfer from large to small scales in turbulence by multiscale nonlinear strain and vorticity interactions," Phys. Rev. Let. **124**, 104501 (2020).

[35] S. Mukherjee, A. Safdari, O. Shardt, S. Kenjereš, and H. E. Van den Akker, "Droplet–turbulence interactions and quasi-equilibrium dynamics in turbulent emulsions," J. Fluid Mech. **878**, 221–276 (2019).

Accepted to Phys. Fluids 10.1063/5.0100334

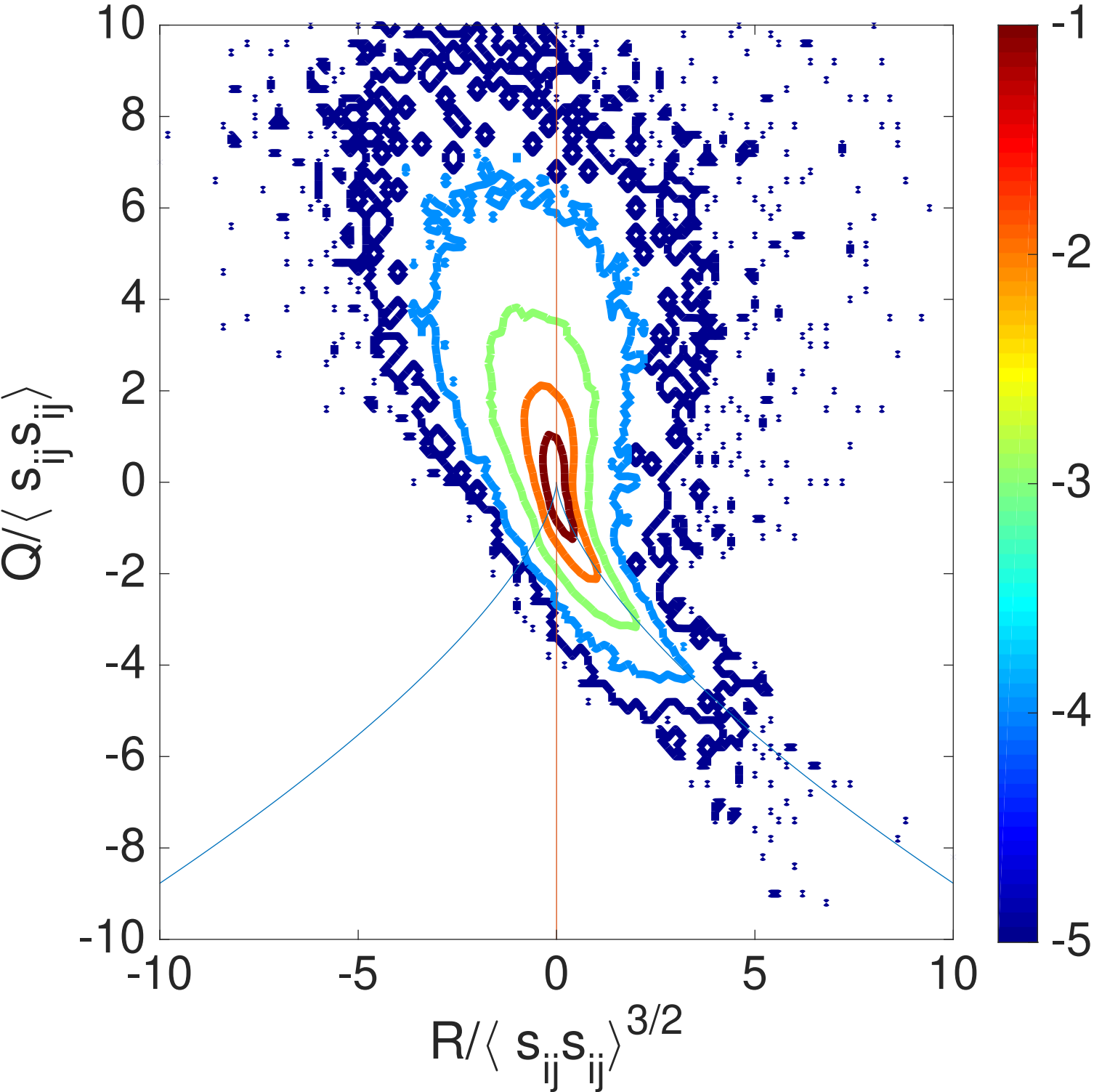

Accepted to Phys. Fluids 10.1063/5.0100334

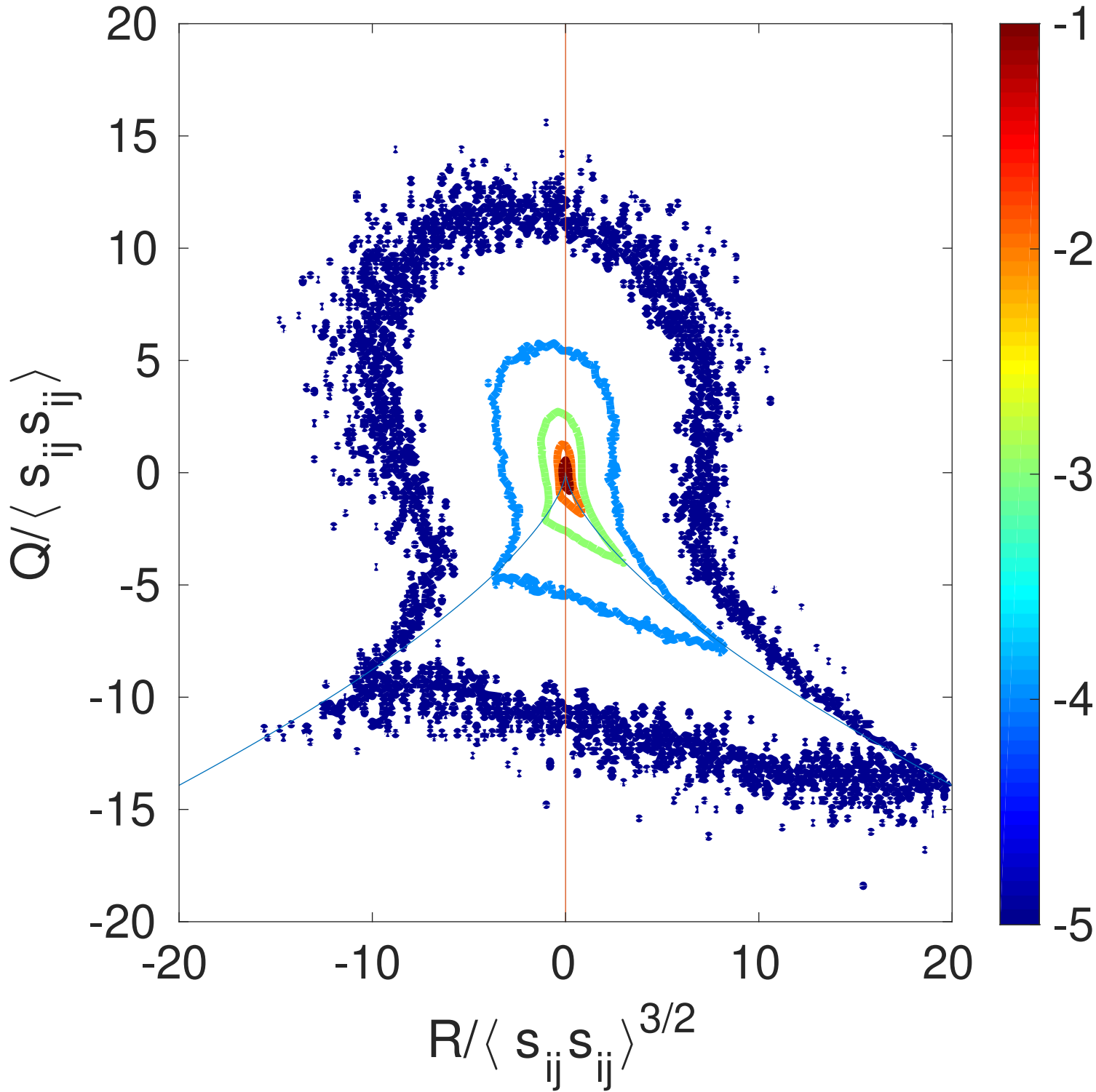

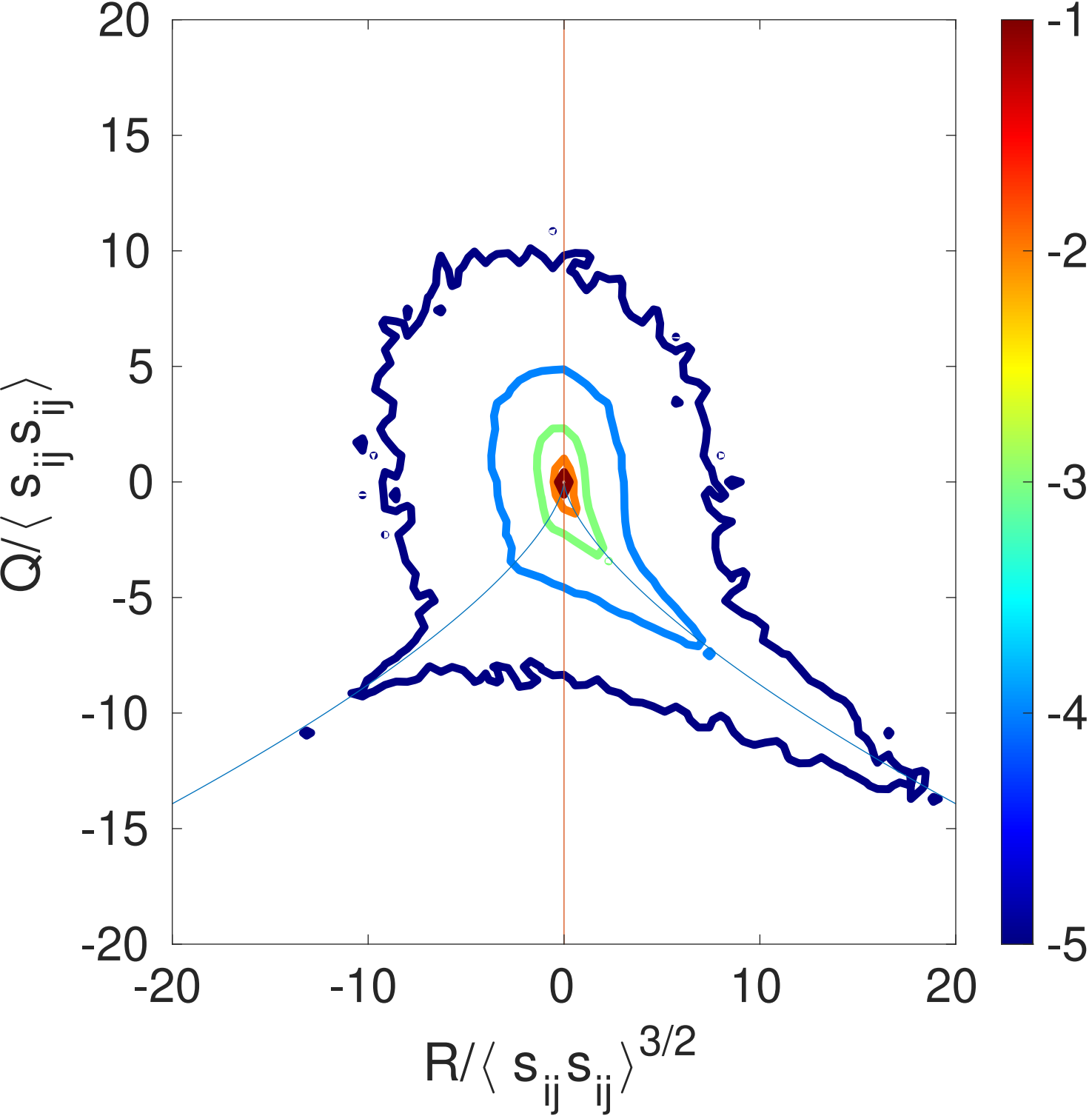
20
15
10
5
0
-5
-10
-15
-20
-20
-10
0
10
20
-1
-2
-3
-4
-5
$Q/\langle s_{ij}s_{ij}\rangle$
$R/\langle s_{ij}s_{ij}\rangle^{3/2}$

Accepted to Phys. Fluids 10.1063/5.0100334

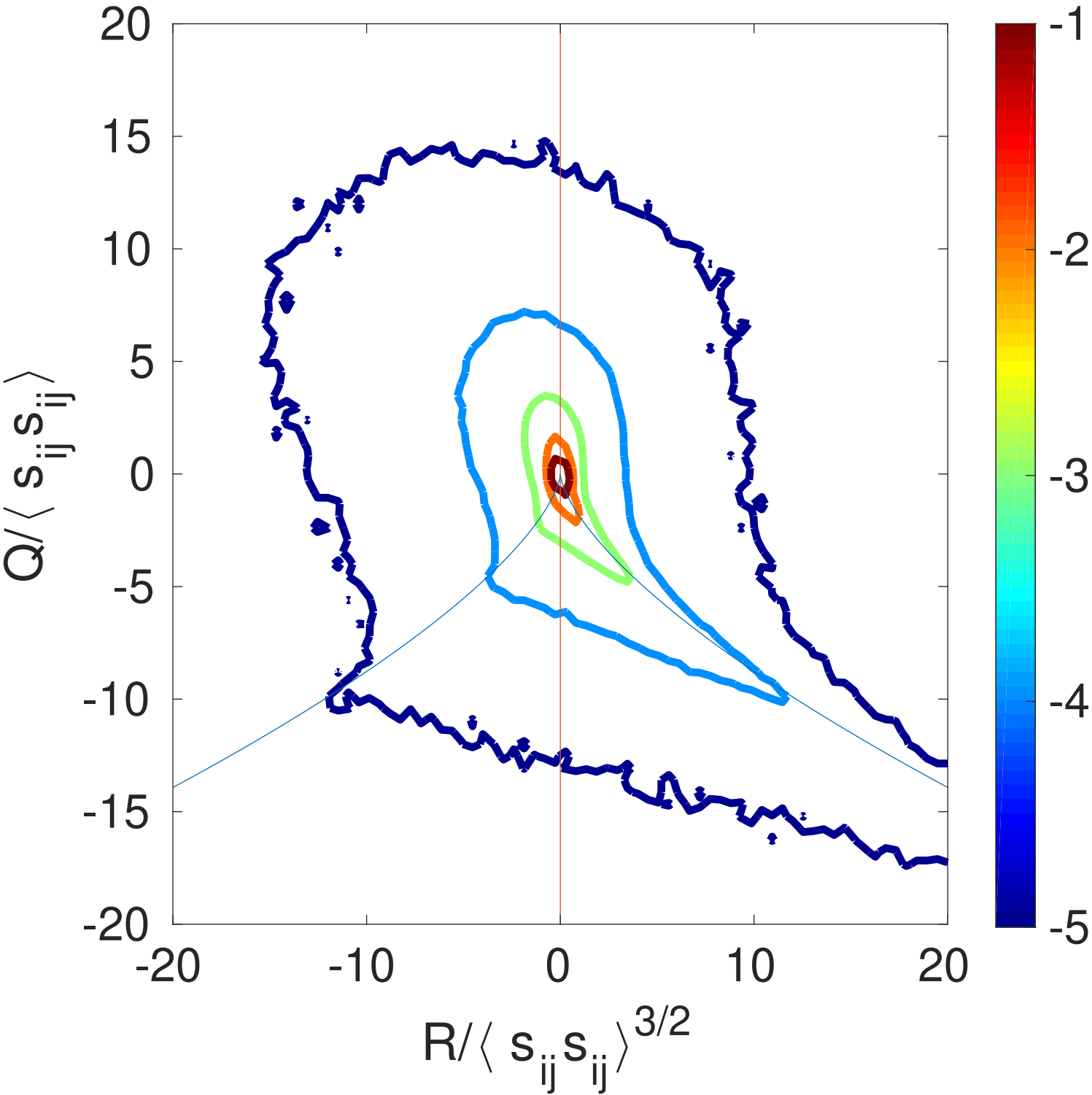

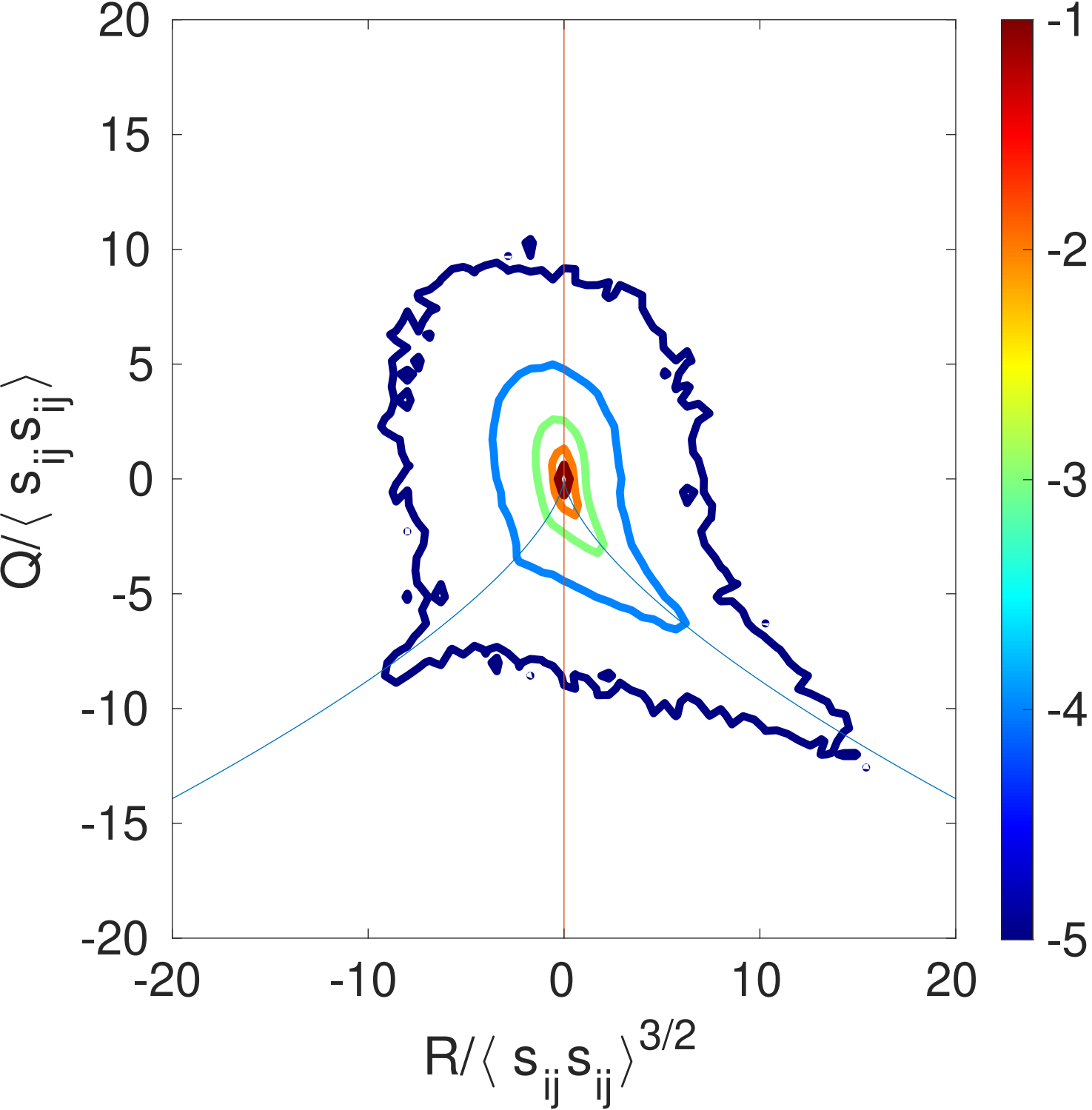
20
15
10
5
0
-5
-10
-15
-20
-20
-10
0
10
20
-1
-2
-3
-4
-5
$Q/\langle s_{ij}s_{ij}\rangle$
$R/\langle s_{ij}s_{ij}\rangle^{3/2}$

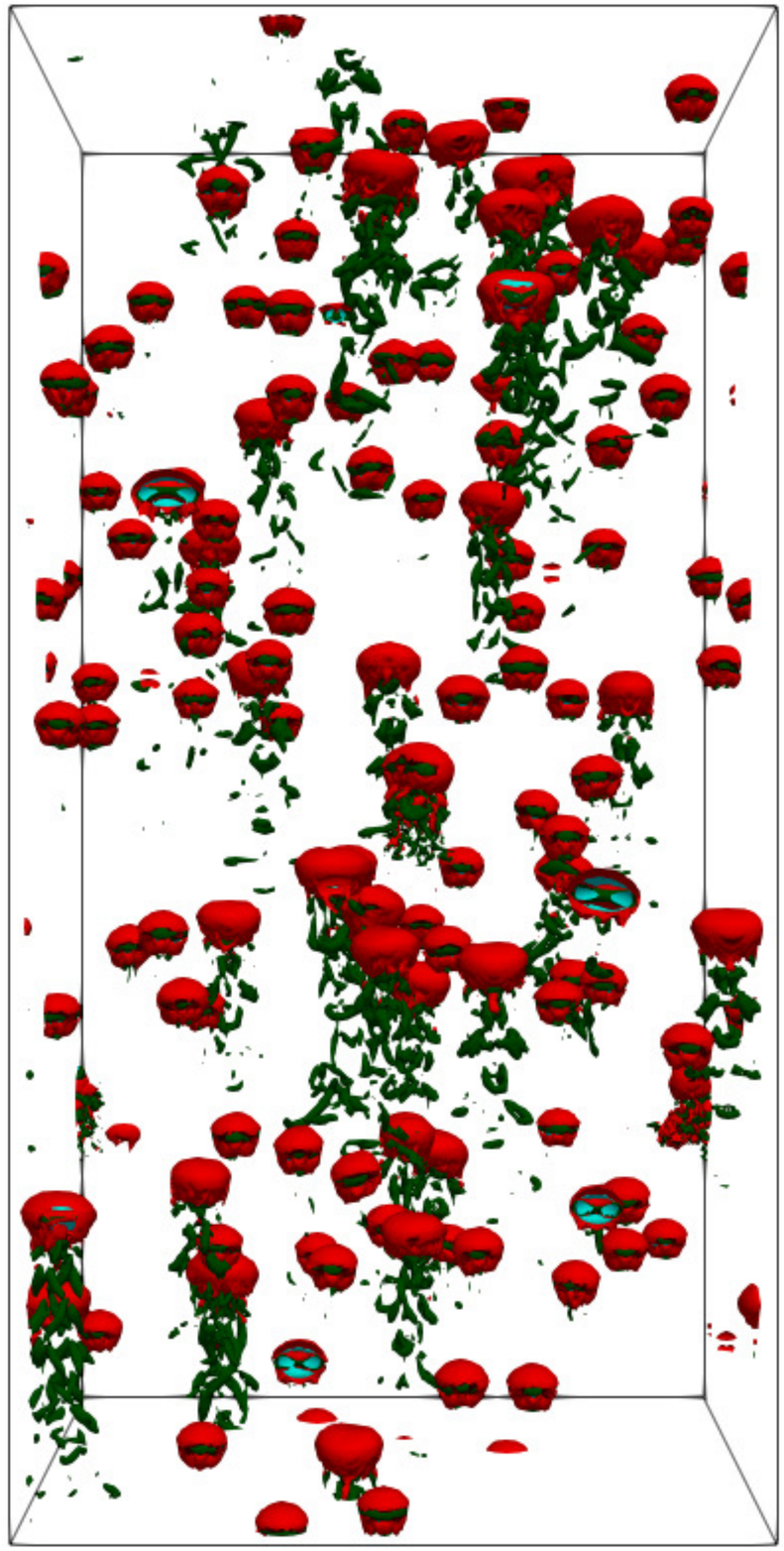
Y
Z
X

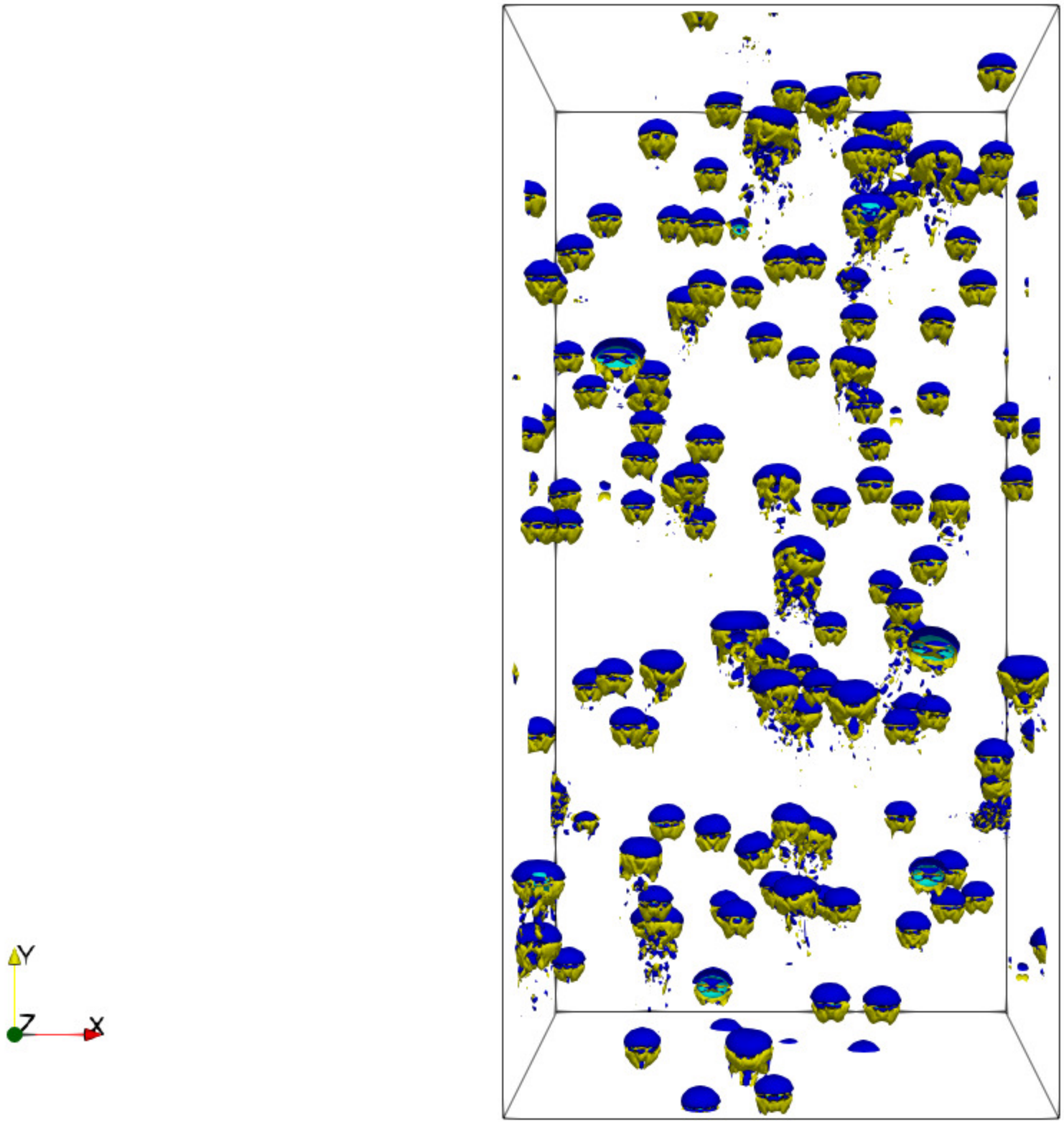
Y
Z
X

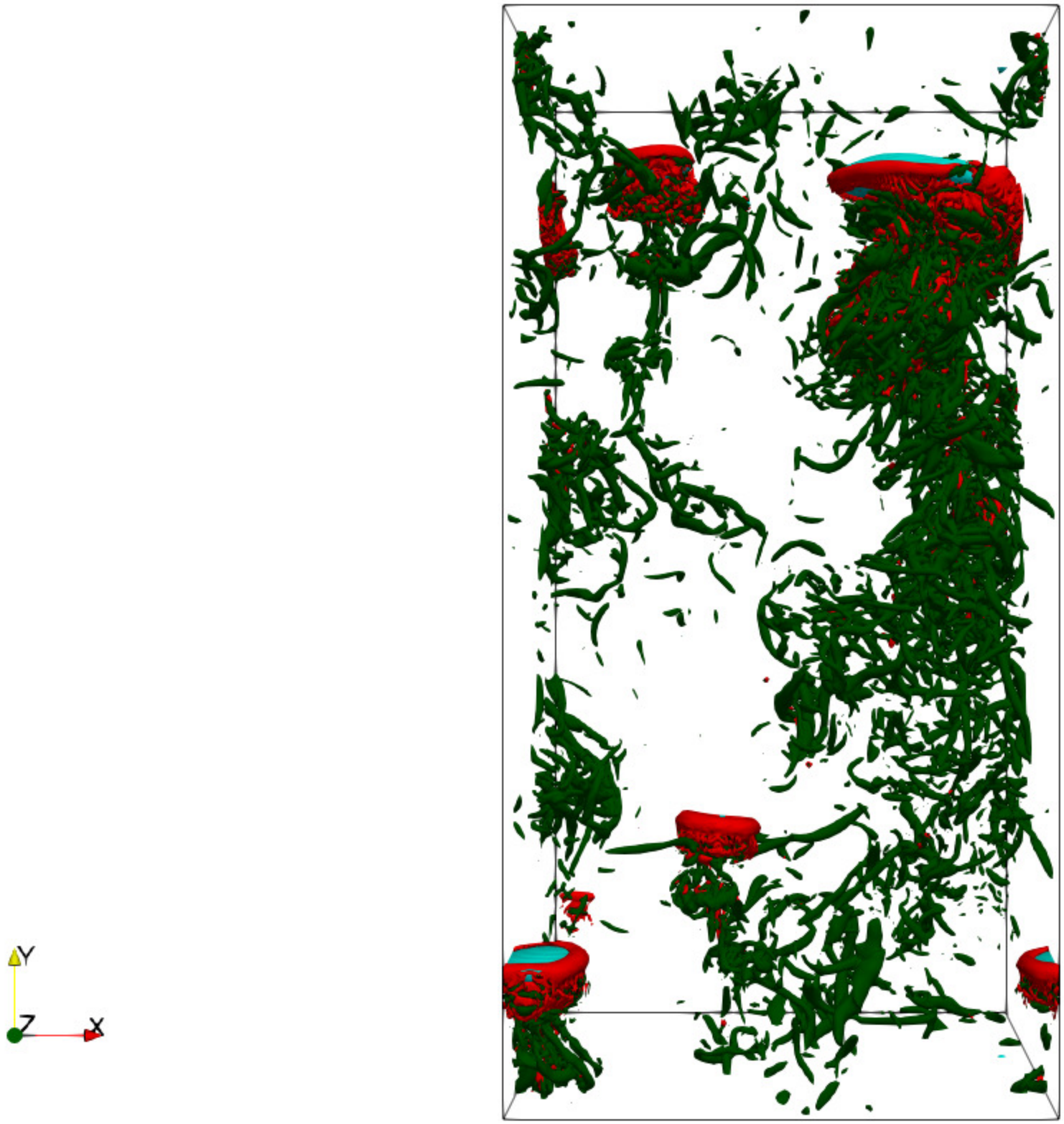
Y
Z
X

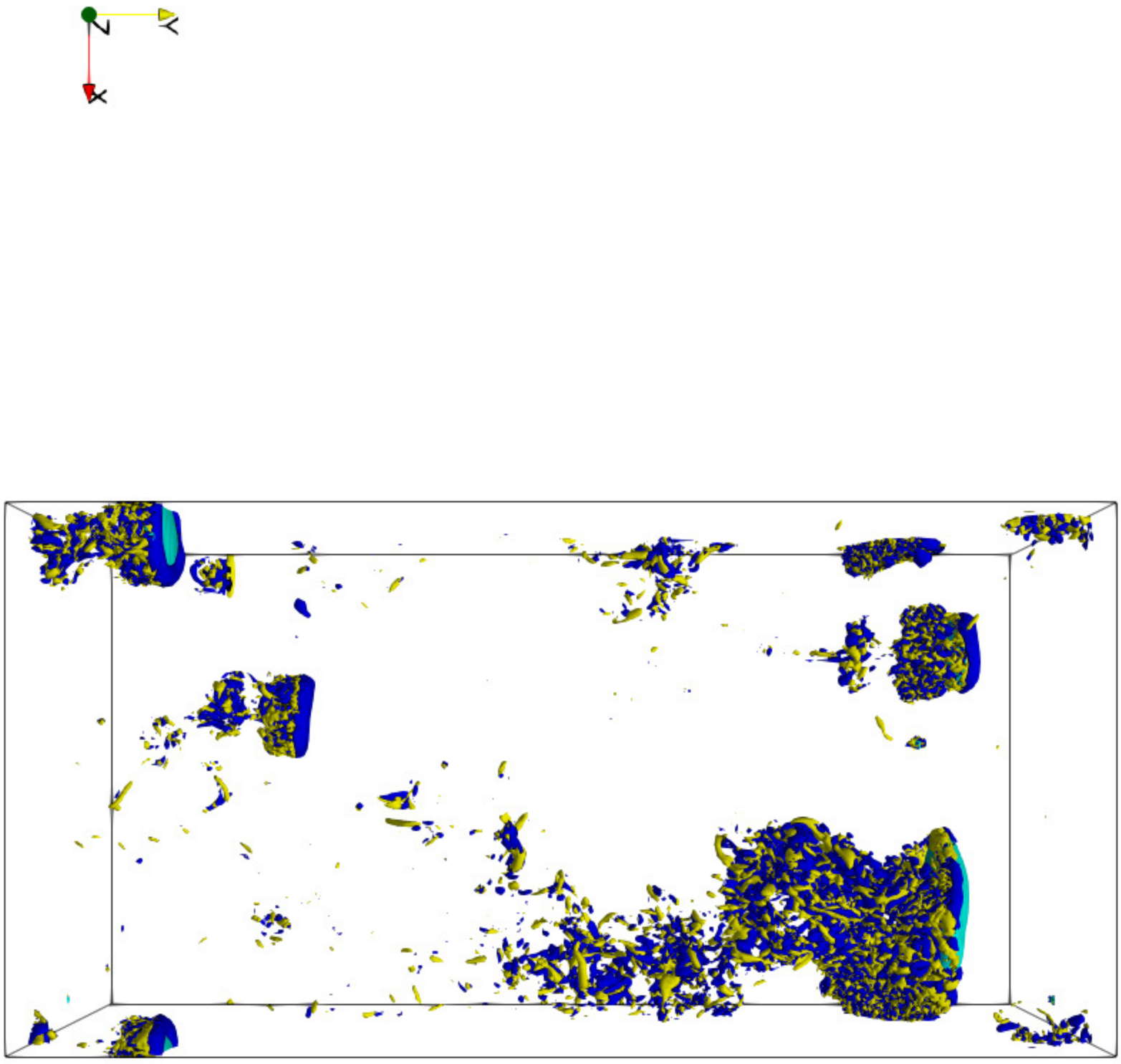
Z
Y
X

Accepted to Phys. Fluids 10.1063/5.0100334

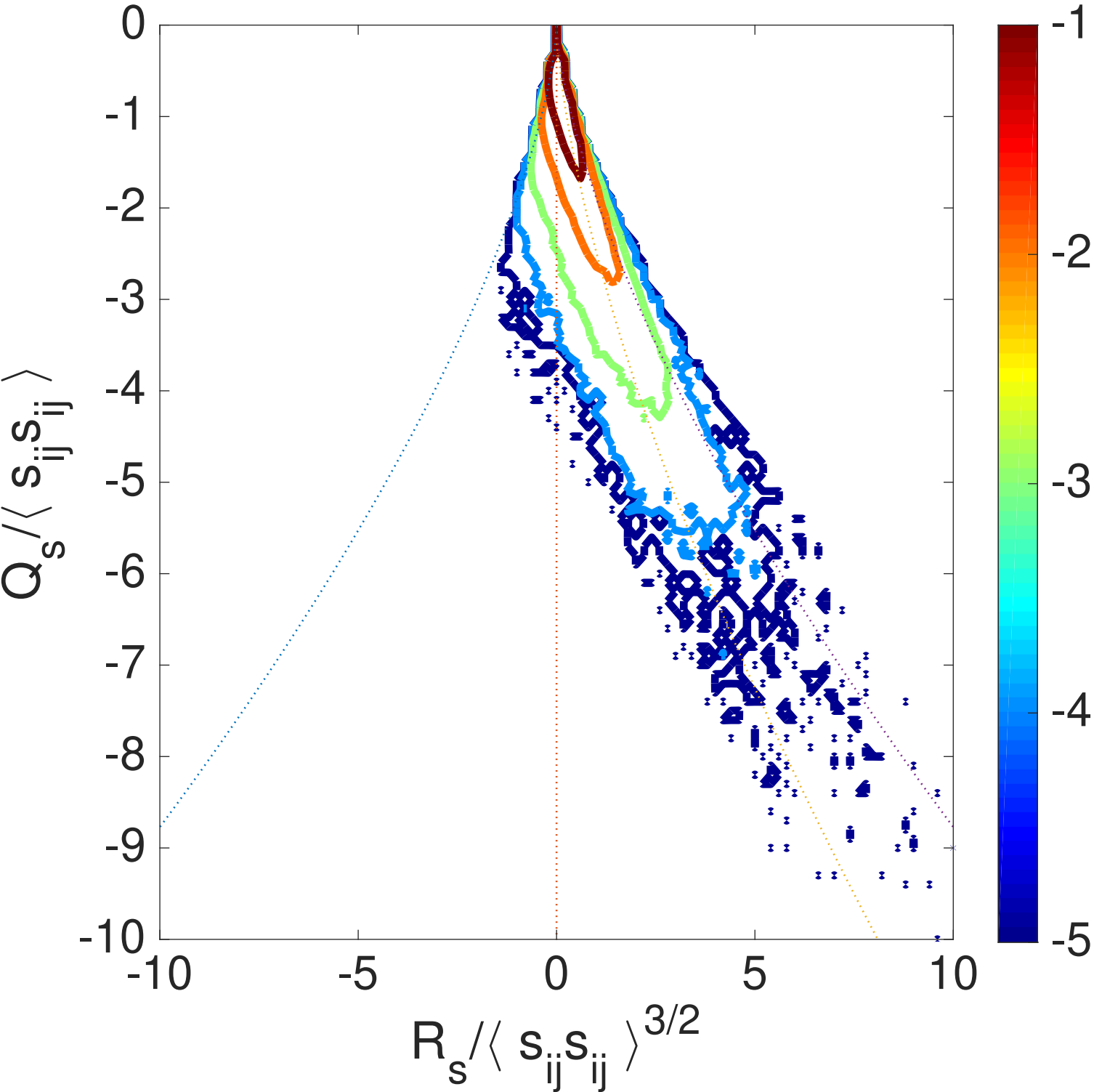

Accepted to Phys. Fluids 10.1063/5.0100334

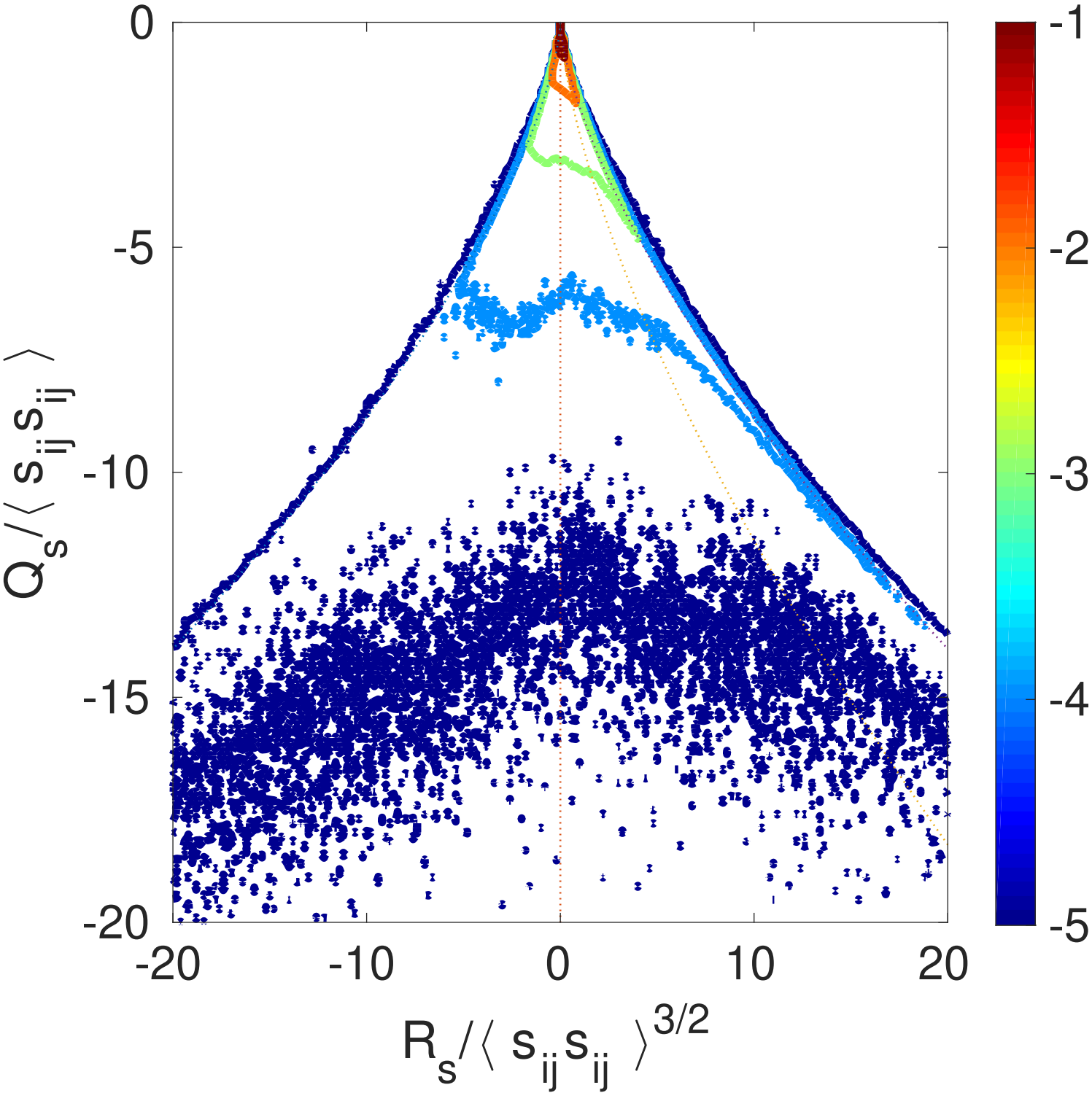

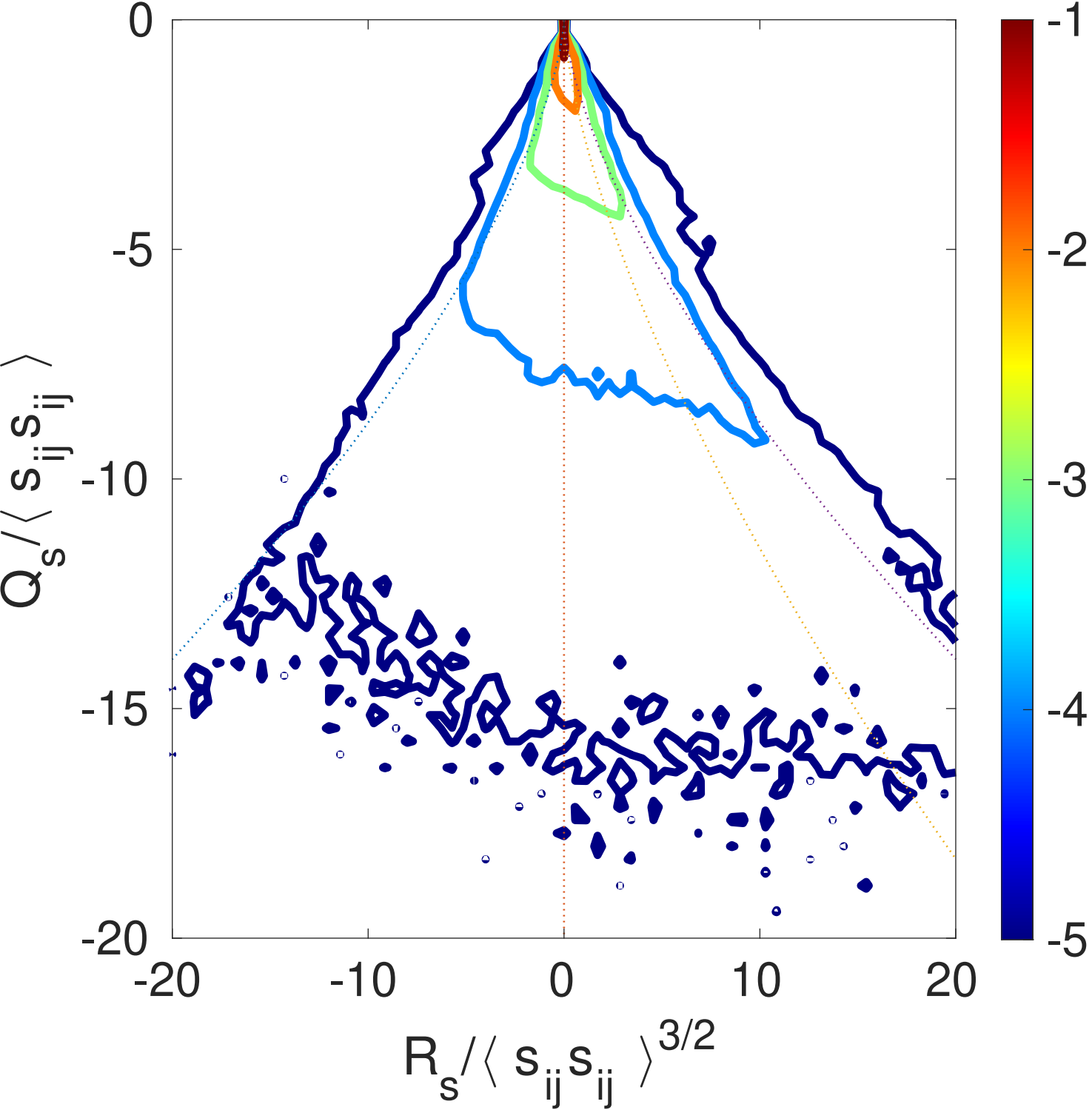
0
-5
-10
-15
-20
-20
-10
0
10
20
-1
-2
-3
-4
-5
$Q_s / \langle s_{ij} s_{ij} \rangle$
$R_s / \langle s_{ij} s_{ij} \rangle^{3/2}$

Accepted to Phys. Fluids 10.1063/5.0100334

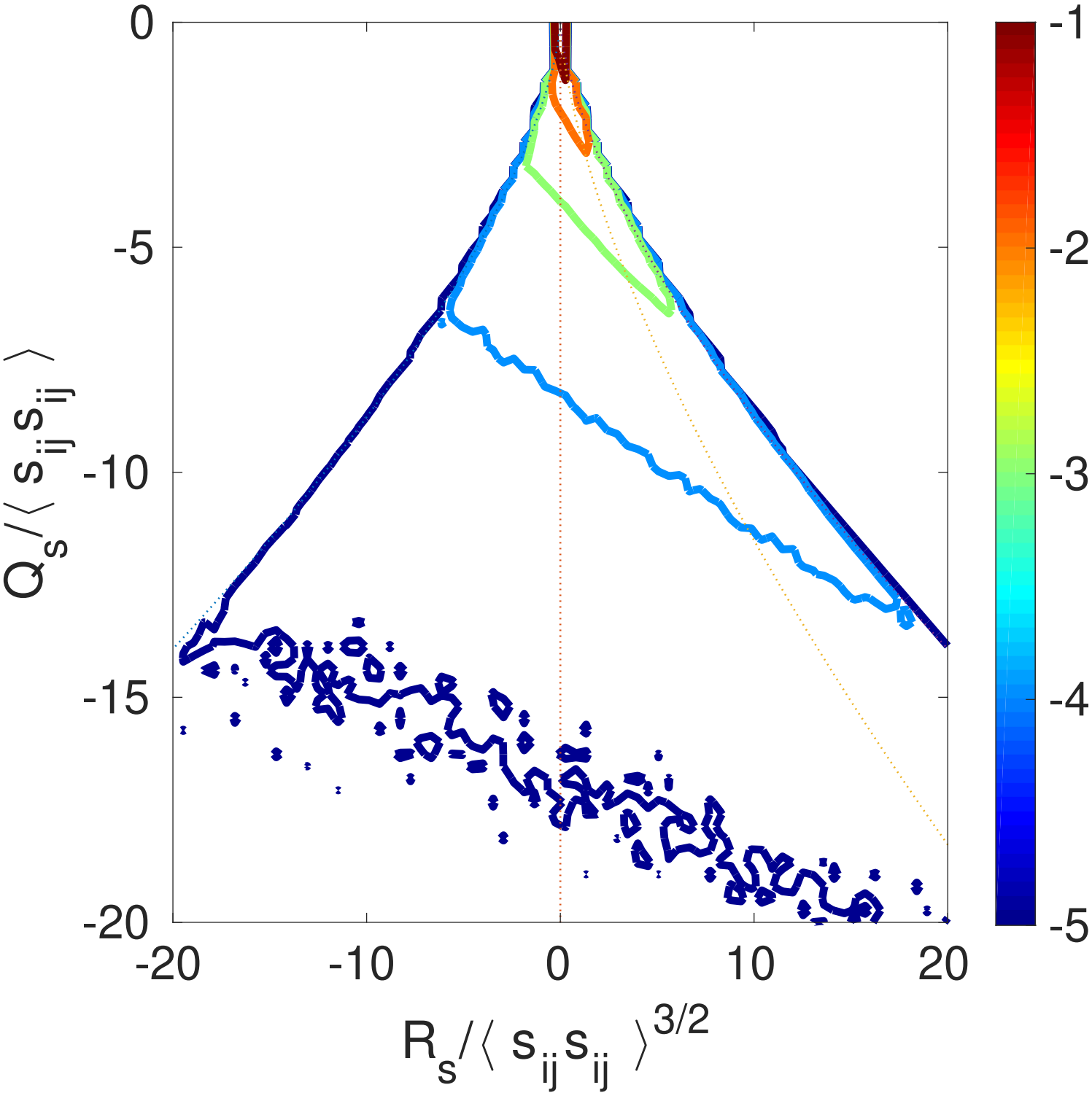

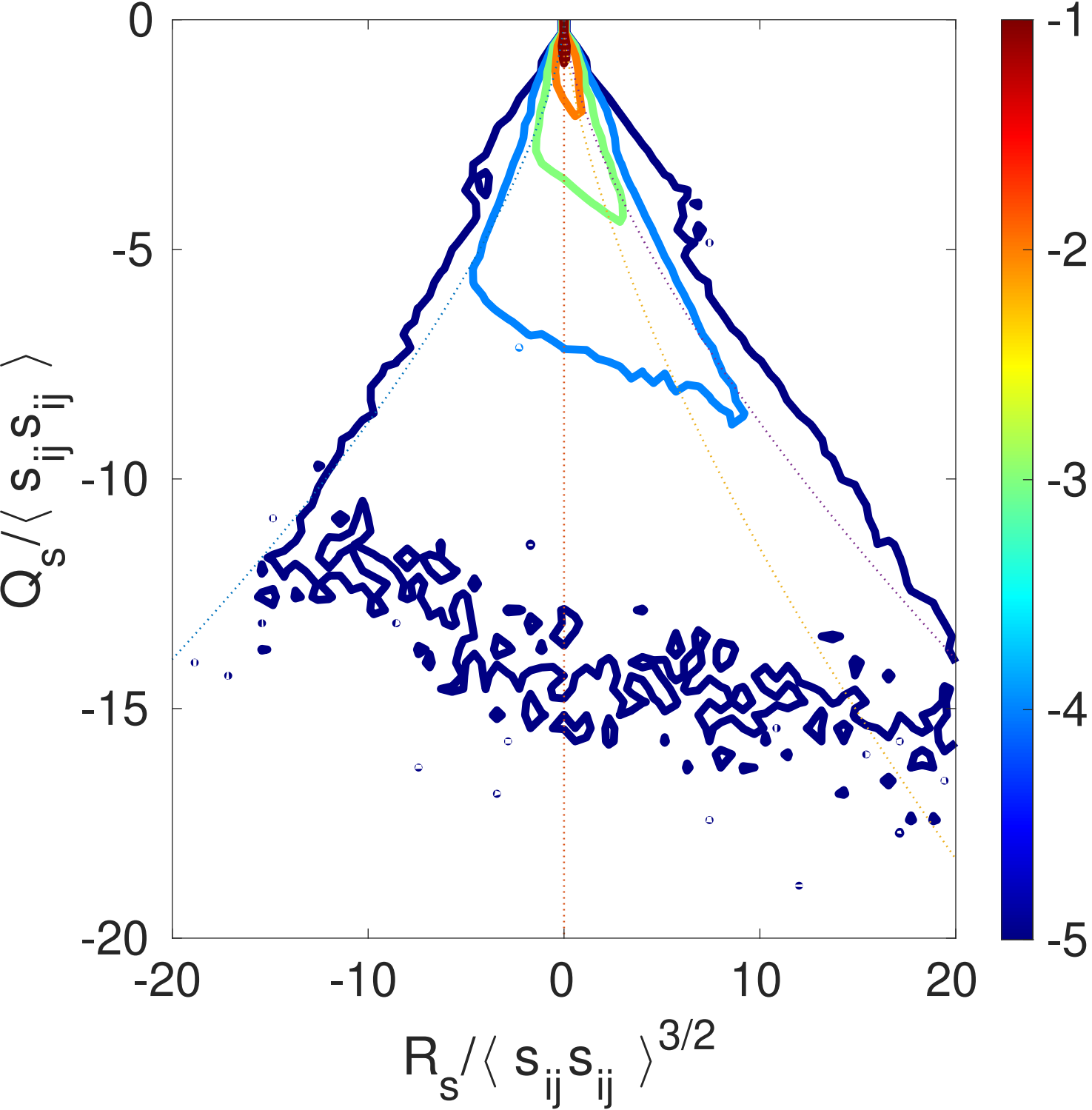
0
-5
-10
-15
-20
-20
-10
0
10
20
-1
-2
-3
-4
-5
$Q_s / \langle s_{ij} s_{ij} \rangle$
$R_s / \langle s_{ij} s_{ij} \rangle^{3/2}$

Accepted to Phys. Fluids 10.1063/5.0100334

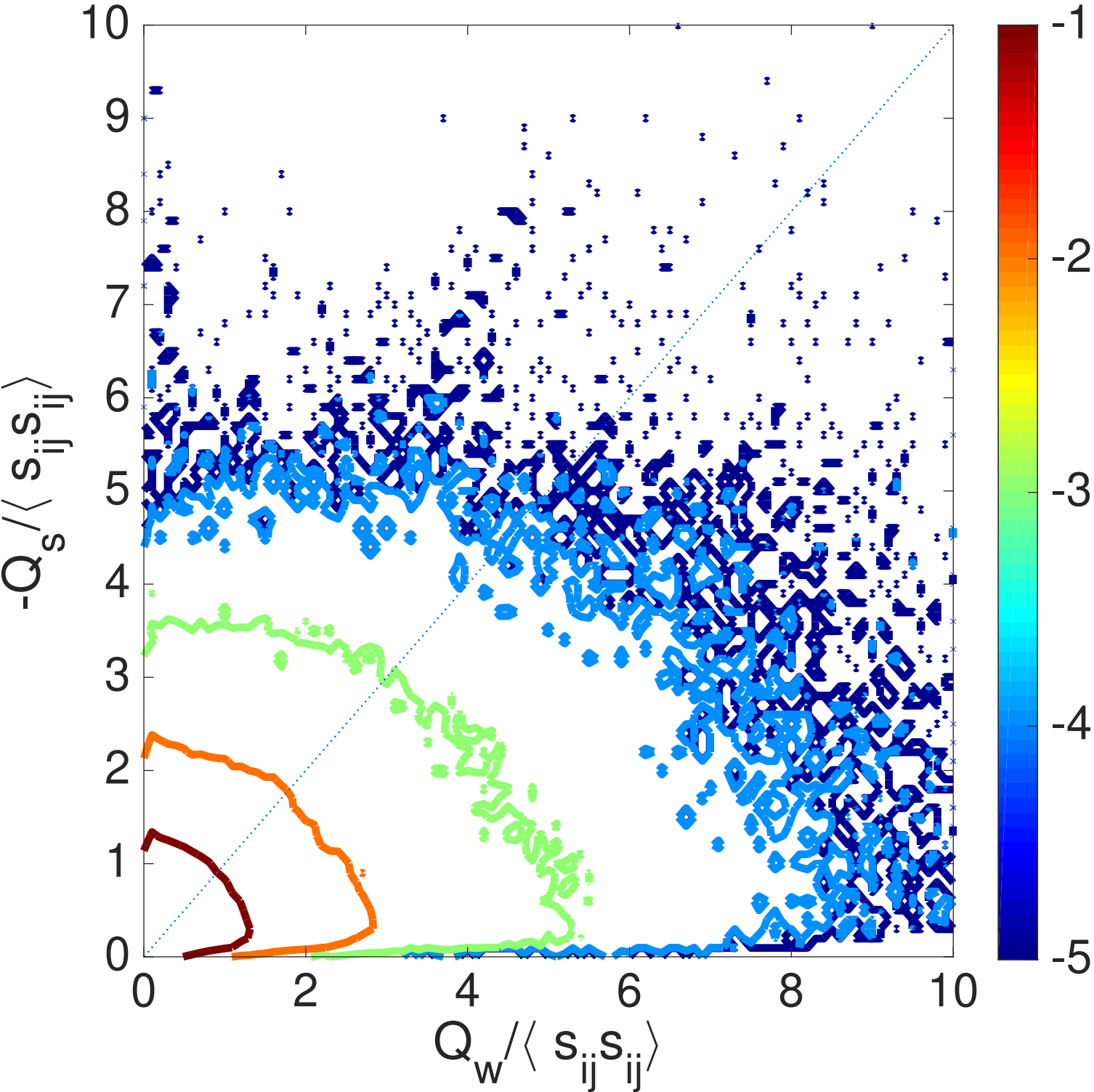

Accepted to Phys. Fluids 10.1063/5.0100334

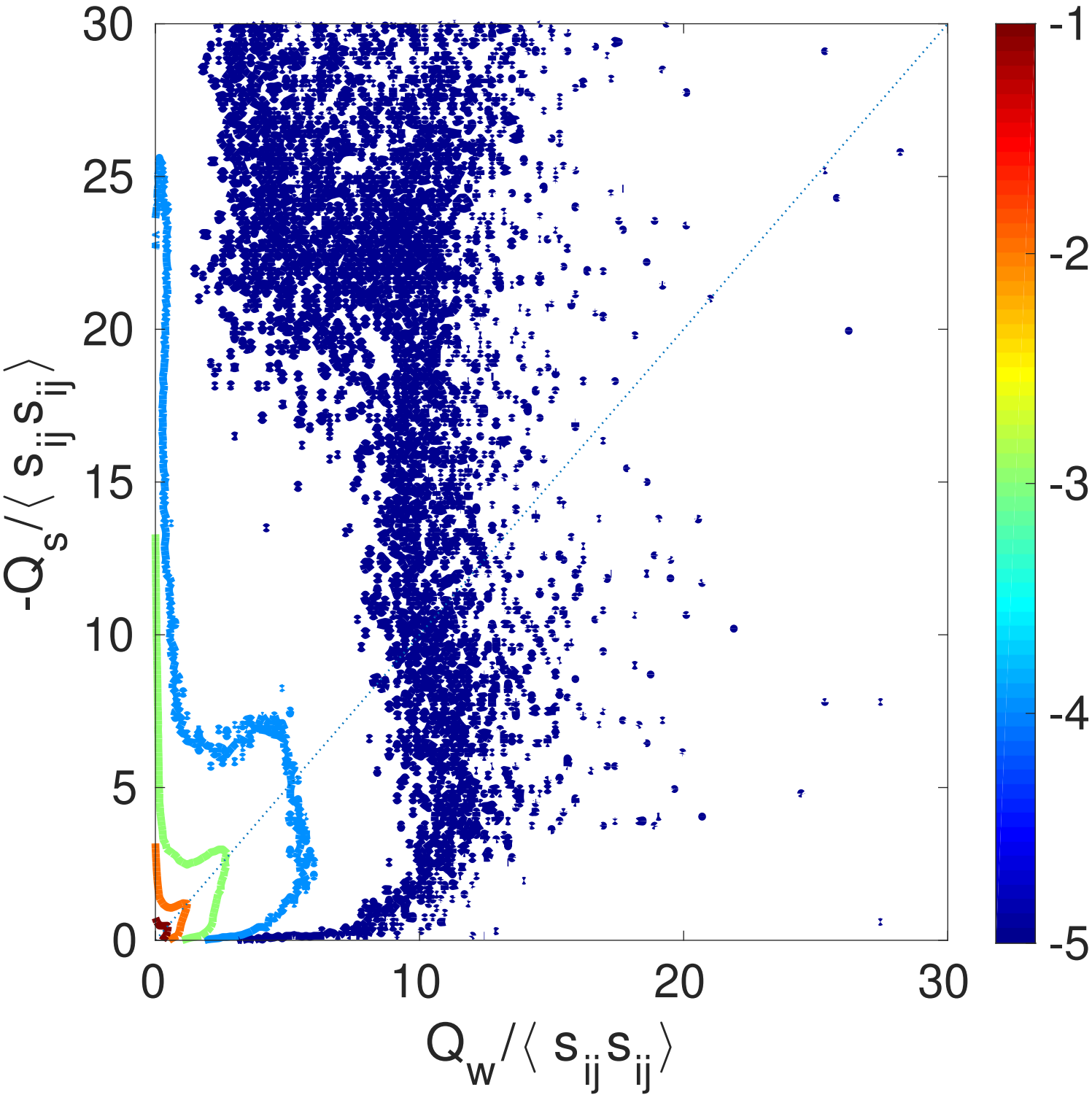

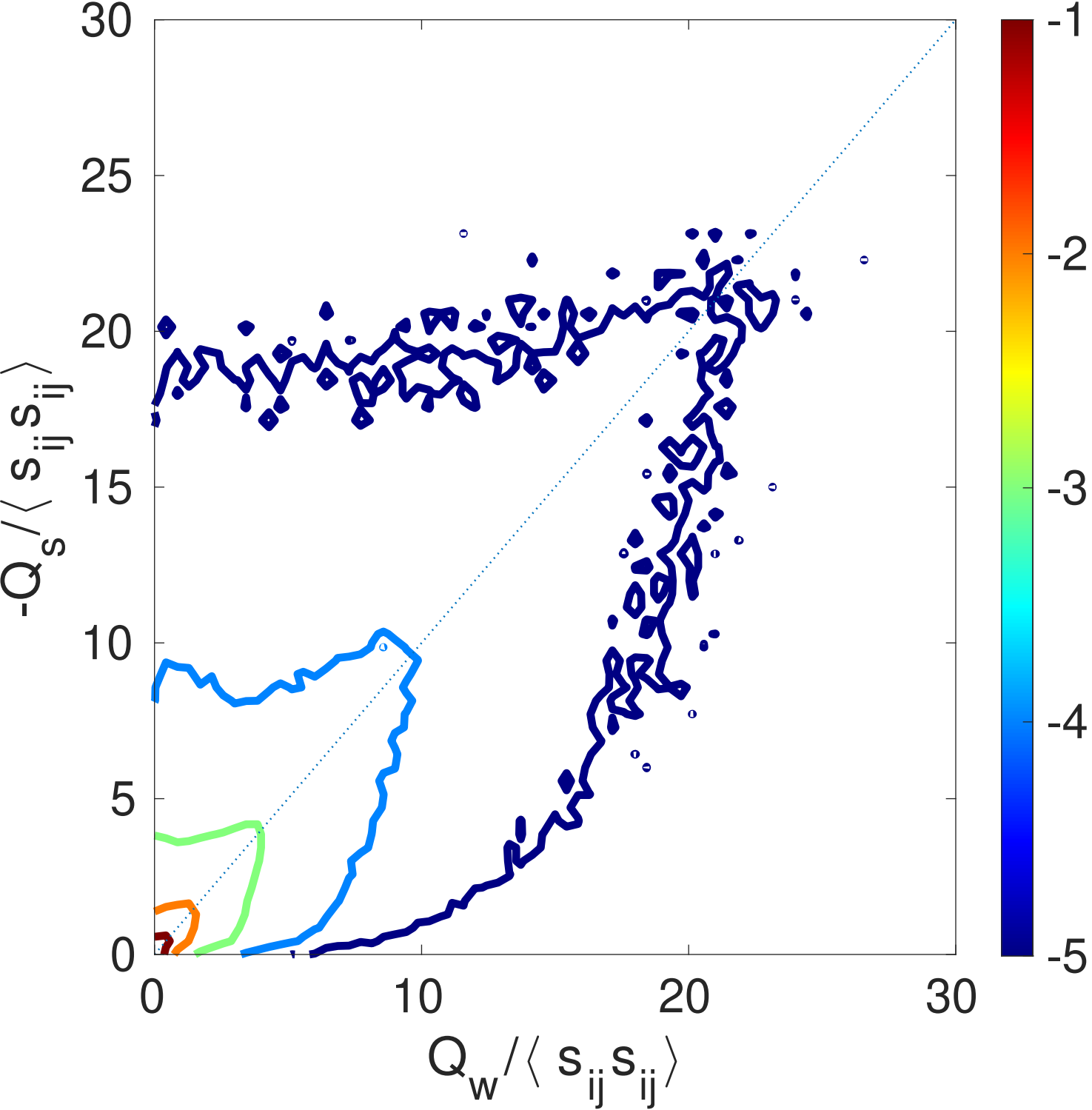
30
25
20
15
10
5
0
0
10
20
30
-1
-2
-3
-4
-5
$-Q_s/\langle s_{ij}s_{ij}\rangle$
$Q_w/\langle s_{ij}s_{ij}\rangle$

Accepted to Phys. Fluids 10.1063/5.0100334

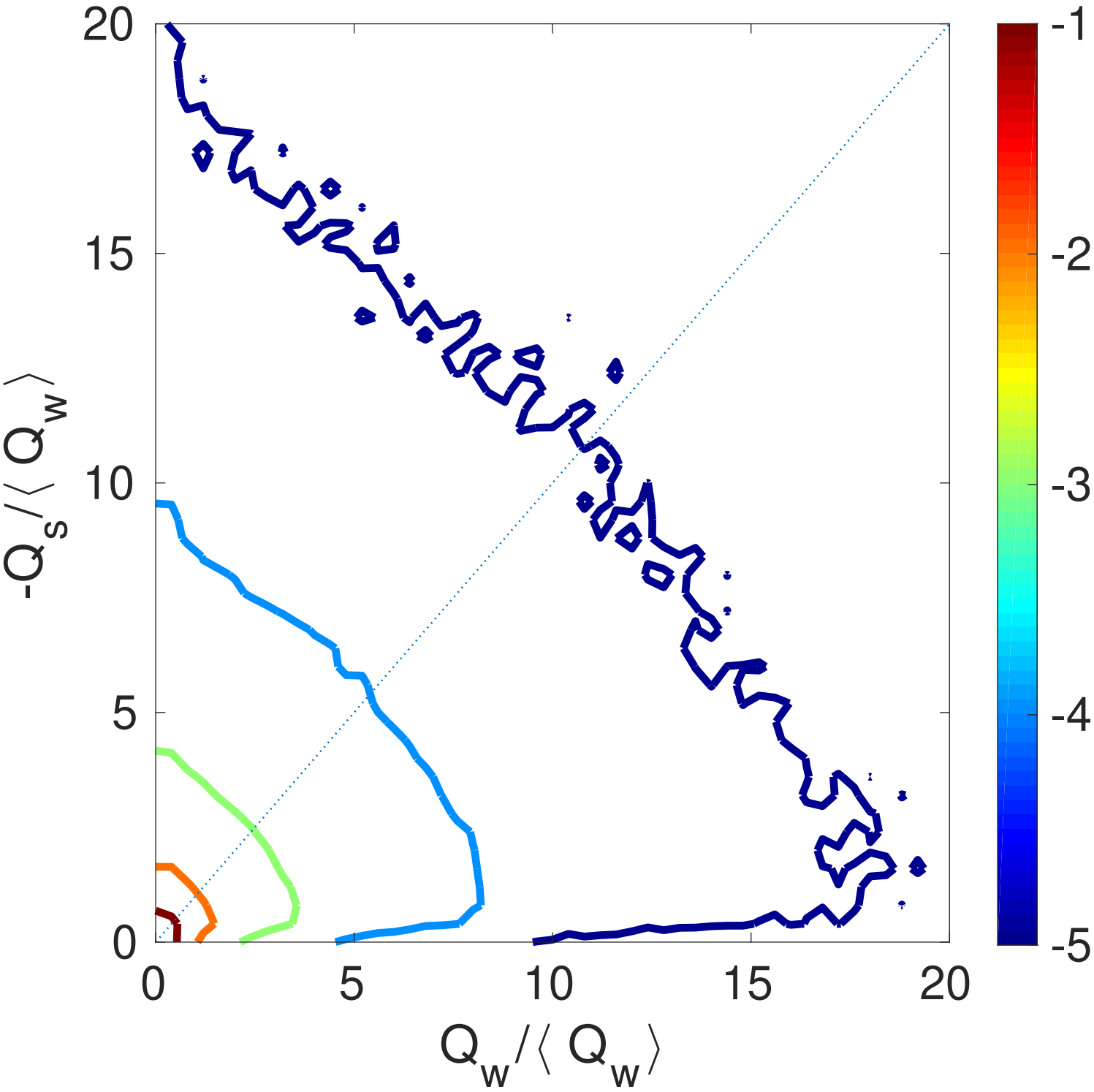

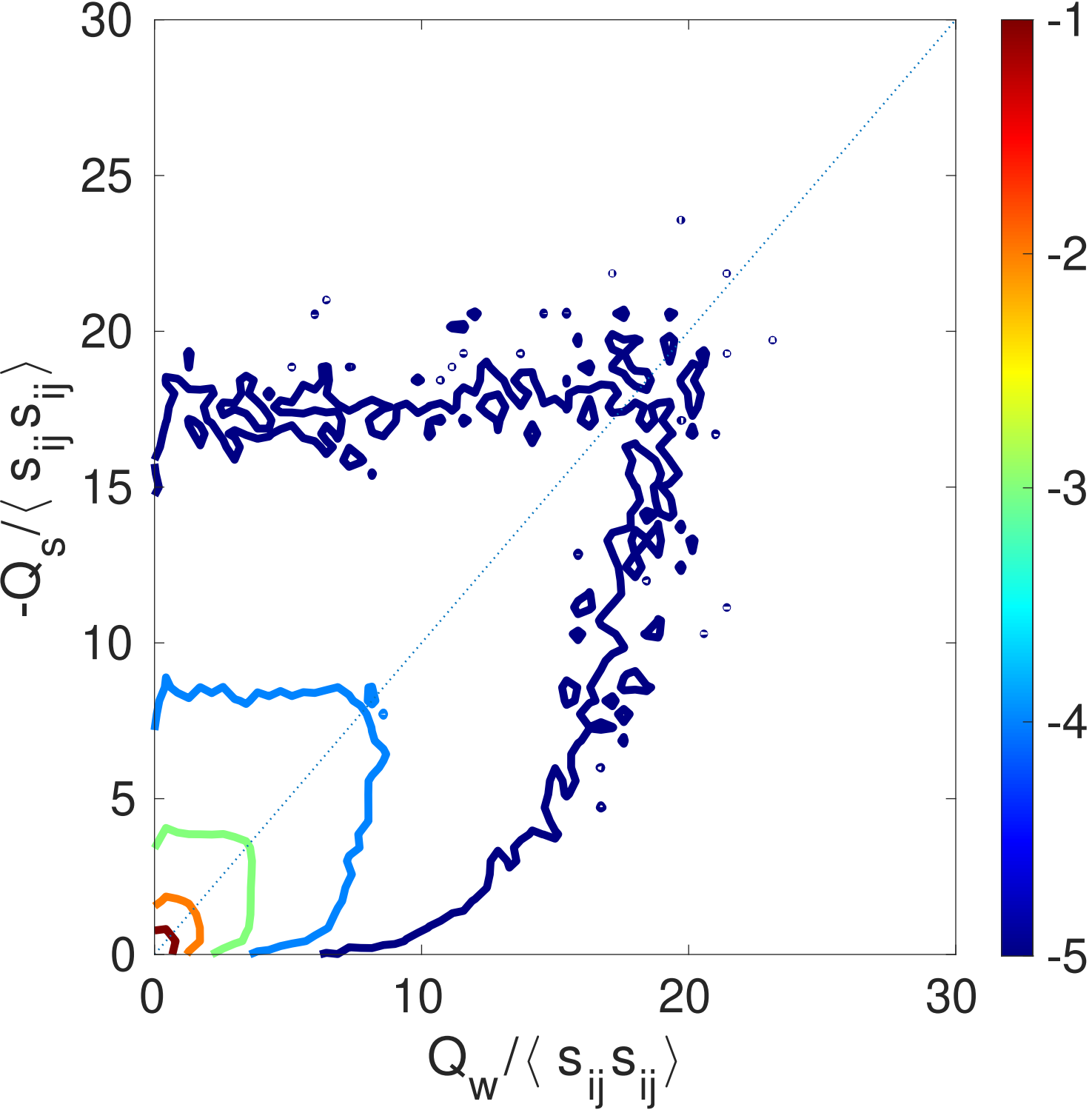
30
25
20
15
10
5
0
0
10
20
30
-1
-2
-3
-4
-5
$-Q_s/\langle s_{ij}s_{ij}\rangle$
$Q_w/\langle s_{ij}s_{ij}\rangle$

Accepted to Phys. Fluids 10.1063/5.0100334

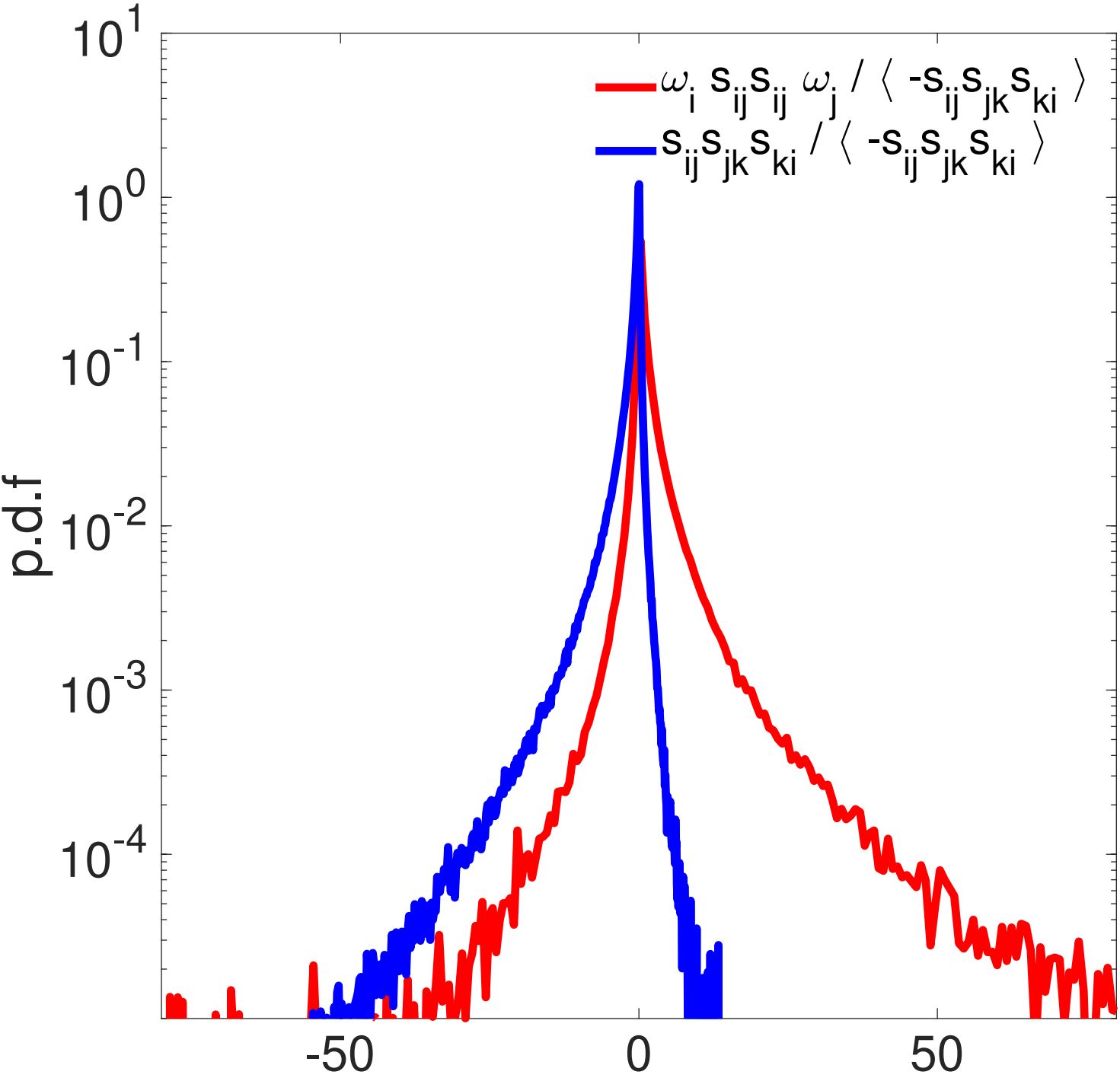

Accepted to Phys. Fluids 10.1063/5.0100334

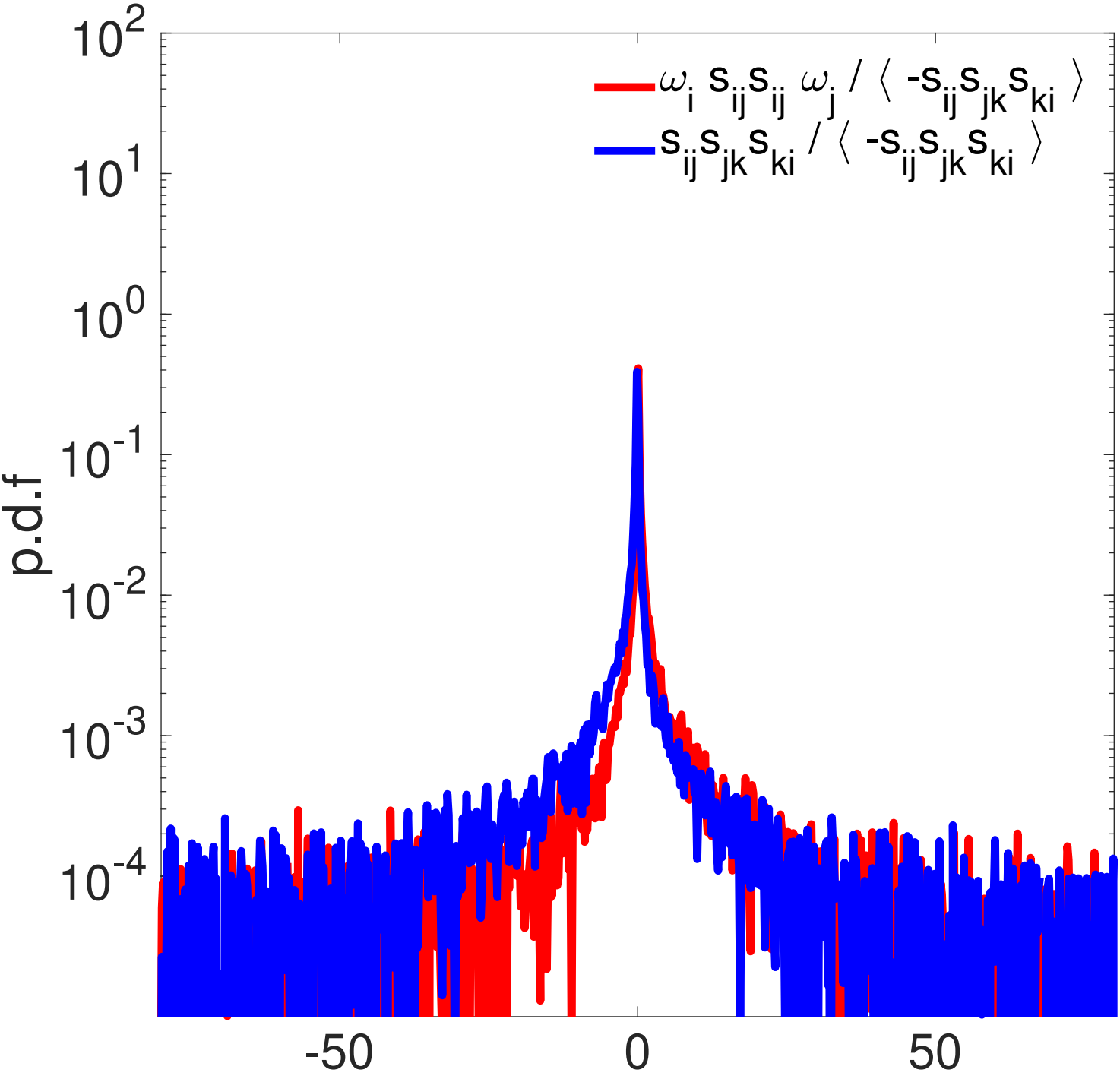

Accepted to Phys. Fluids 10.1063/5.0100334

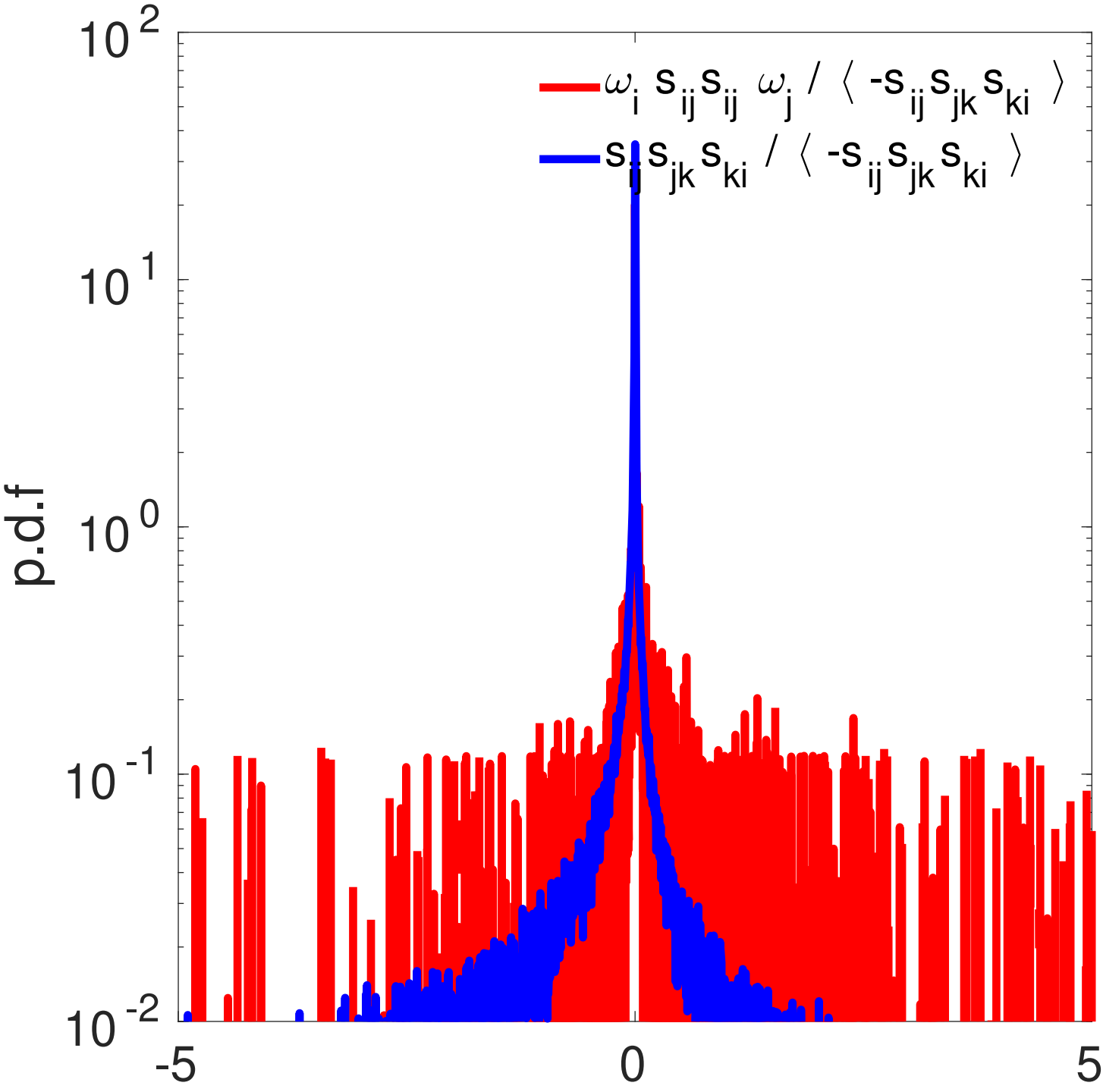

Accepted to Phys. Fluids 10.1063/5.0100334

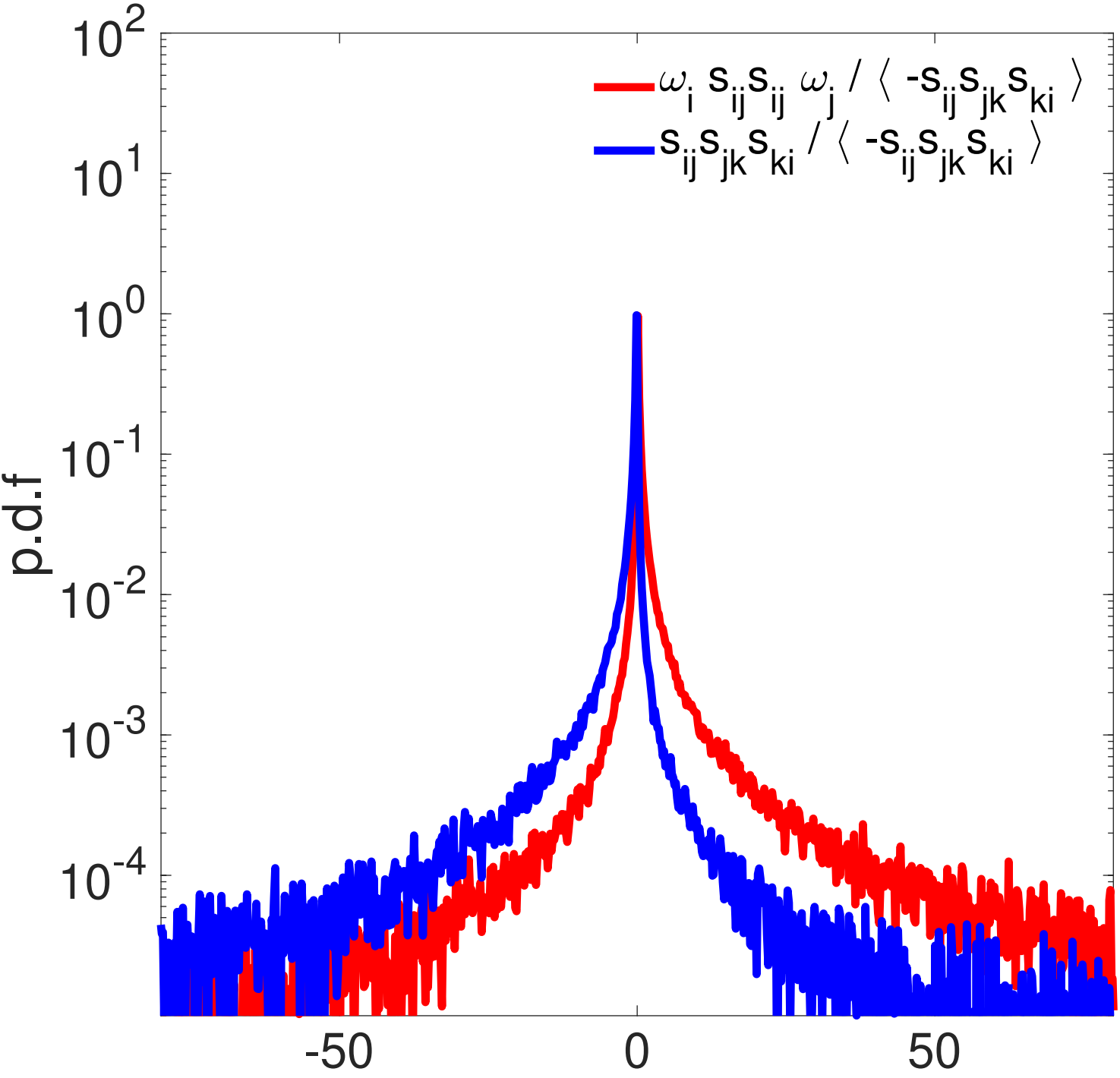

Accepted to Phys. Fluids 10.1063/5.0100334

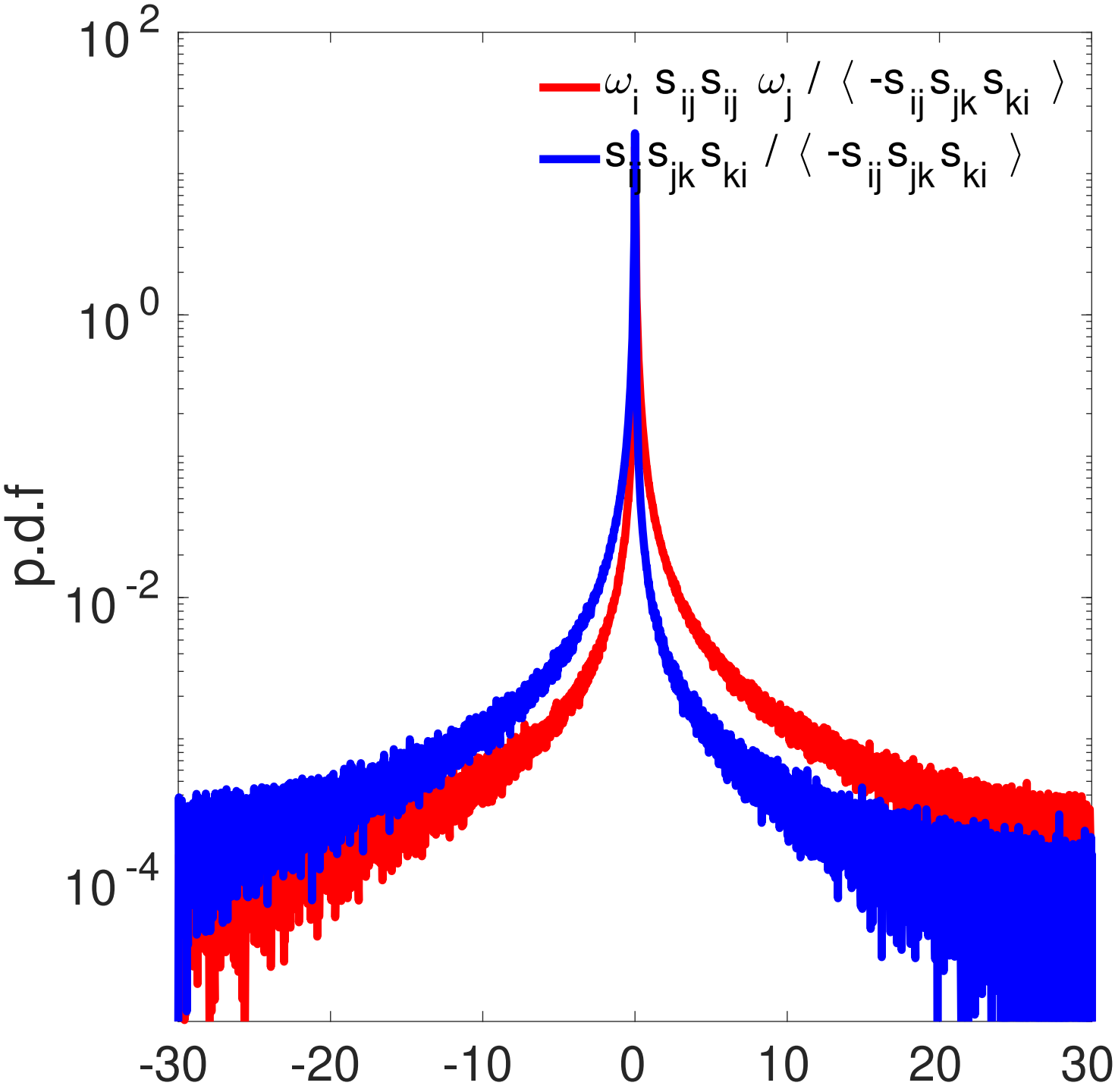

Accepted to Phys. Fluids 10.1063/5.0100334

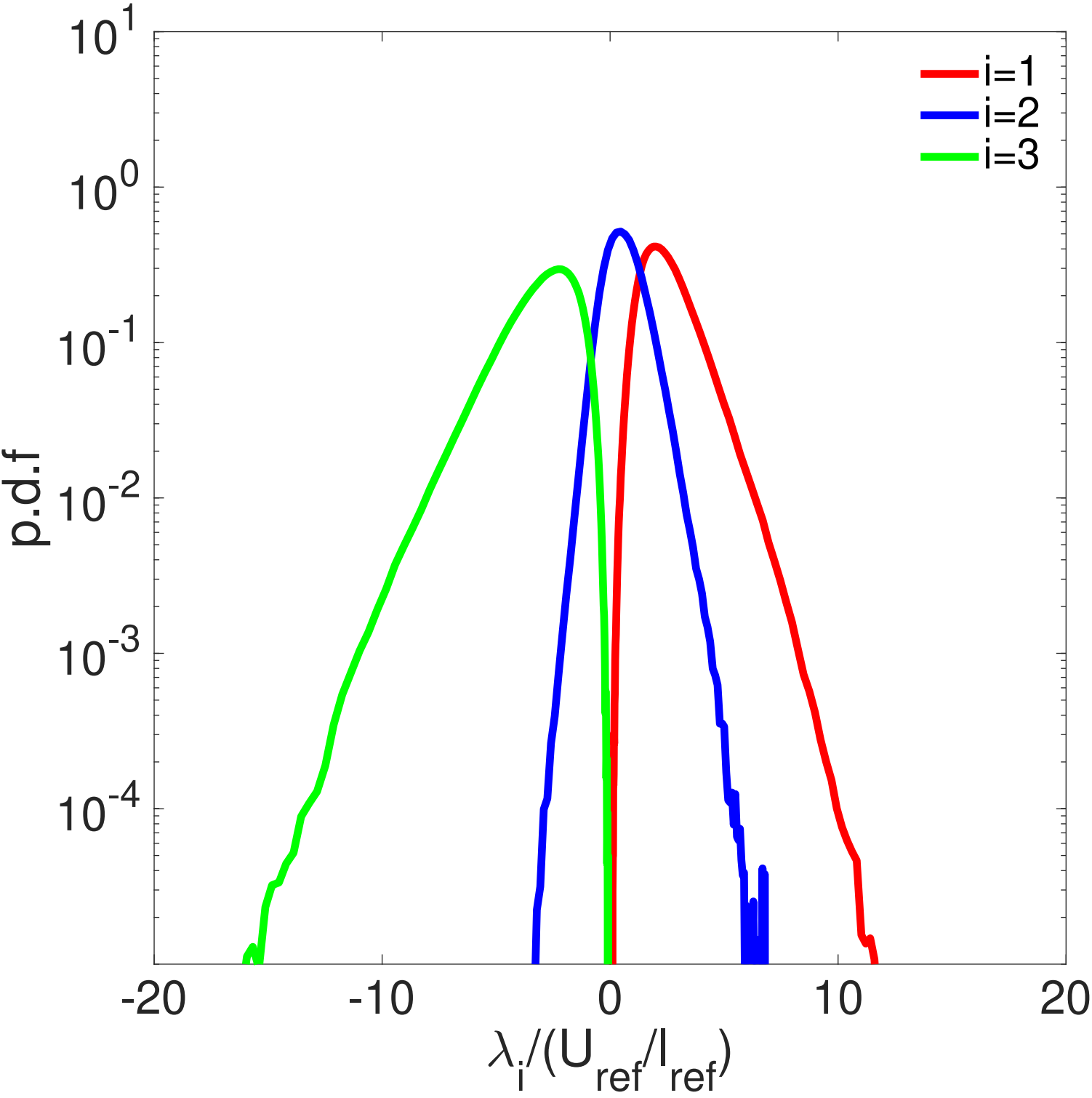

Accepted to Phys. Fluids 10.1063/5.0100334

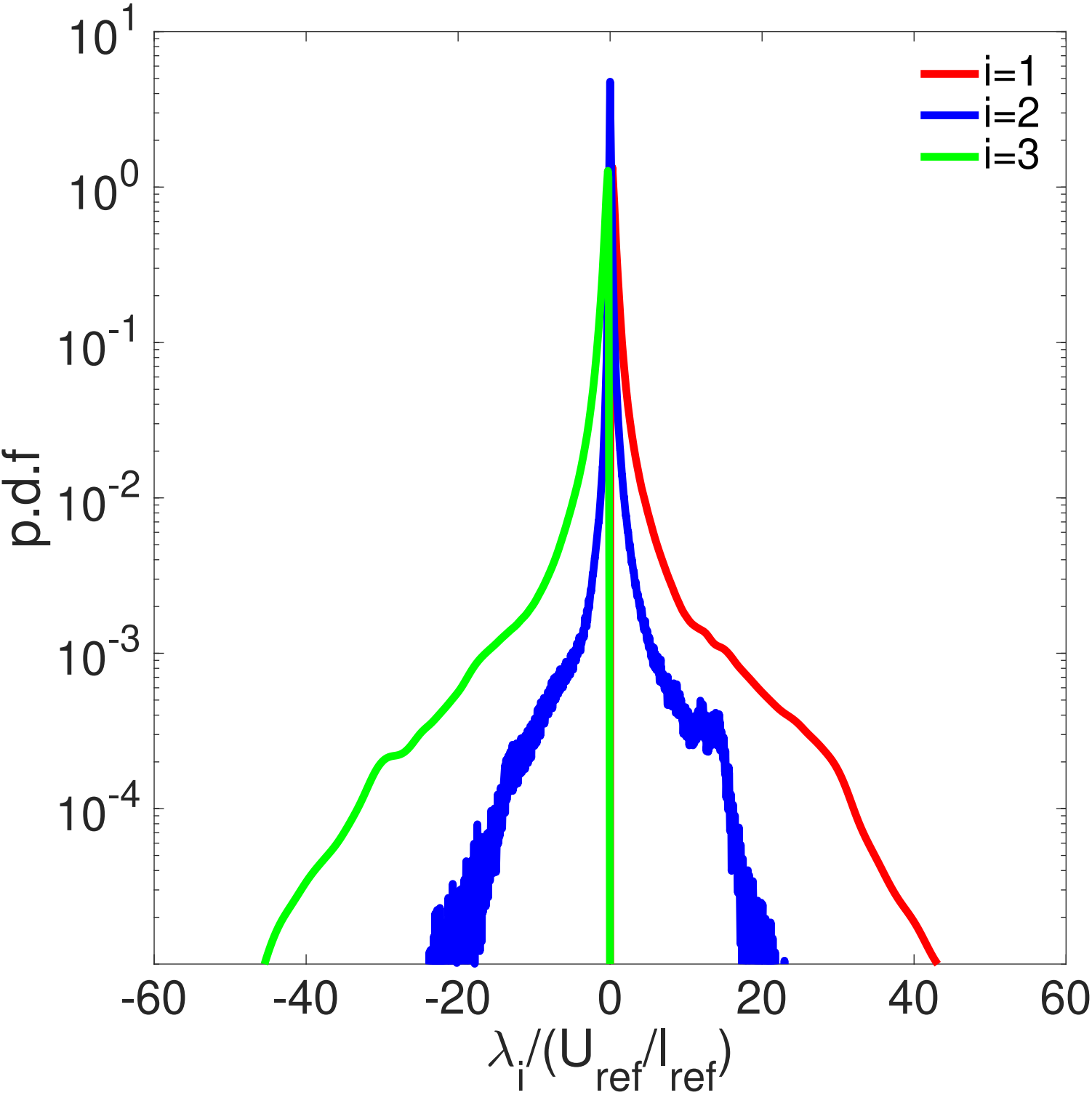

Accepted to Phys. Fluids 10.1063/5.0100334

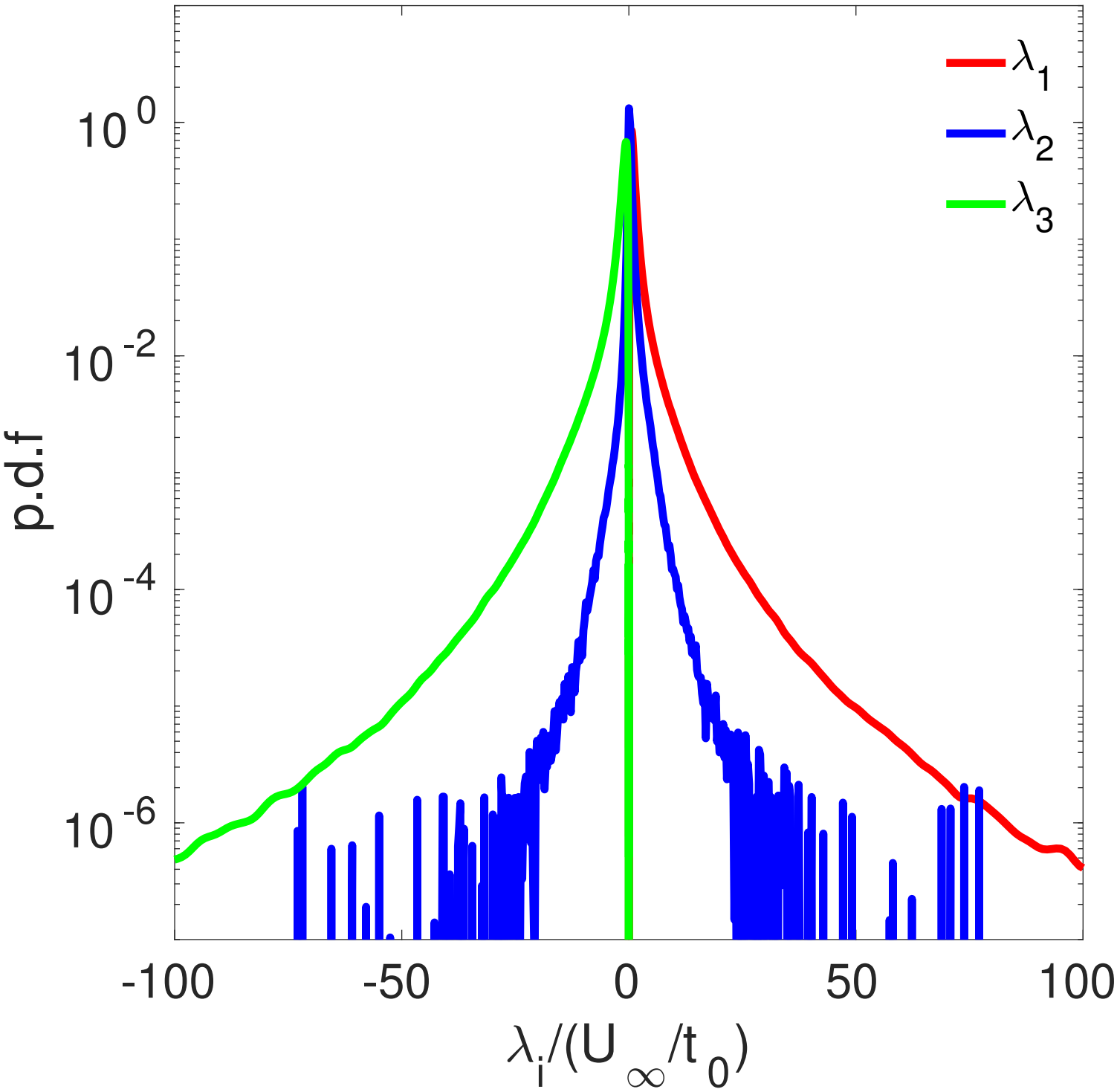

Accepted to Phys. Fluids 10.1063/5.0100334

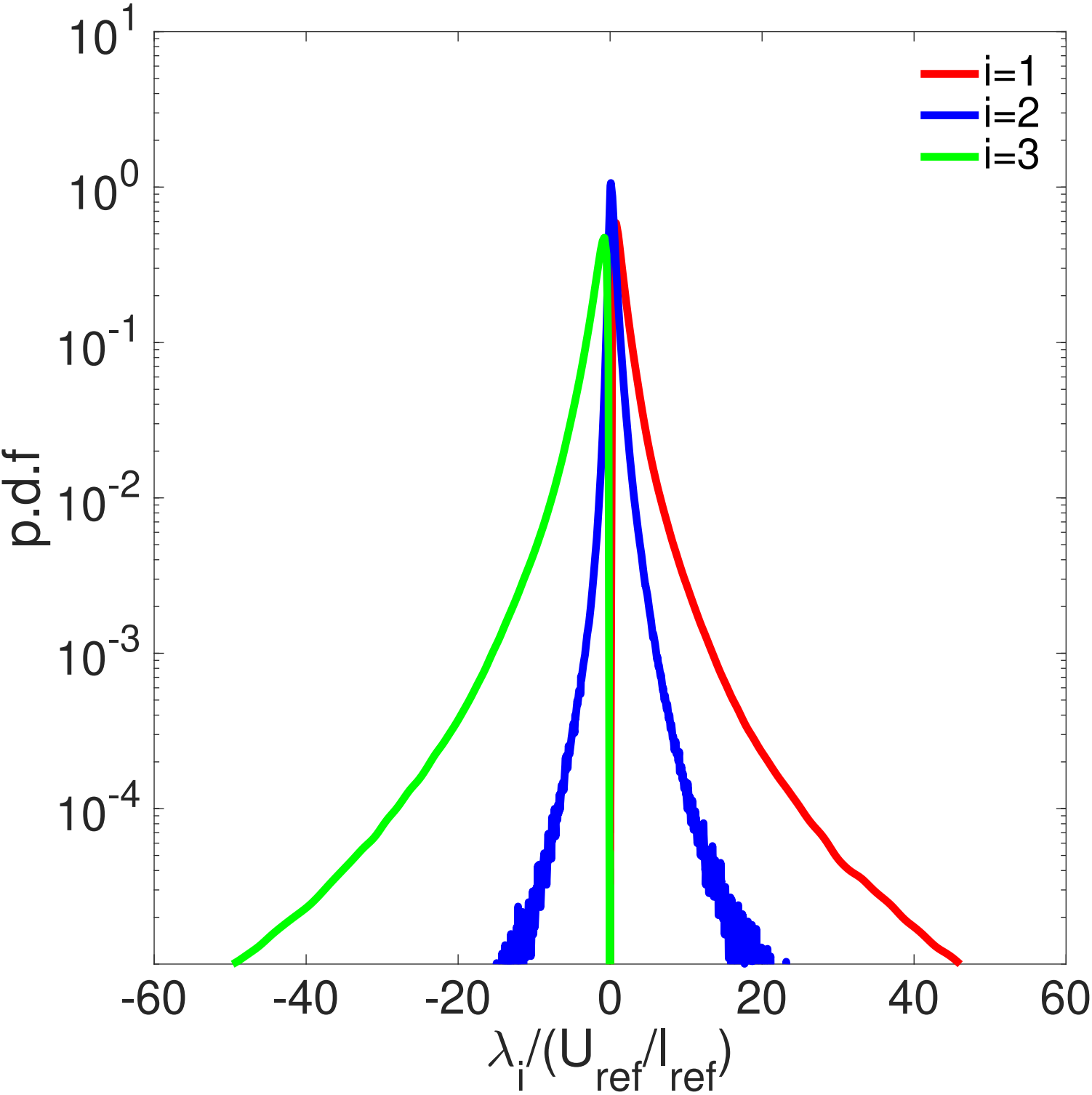

Accepted to Phys. Fluids 10.1063/5.0100334

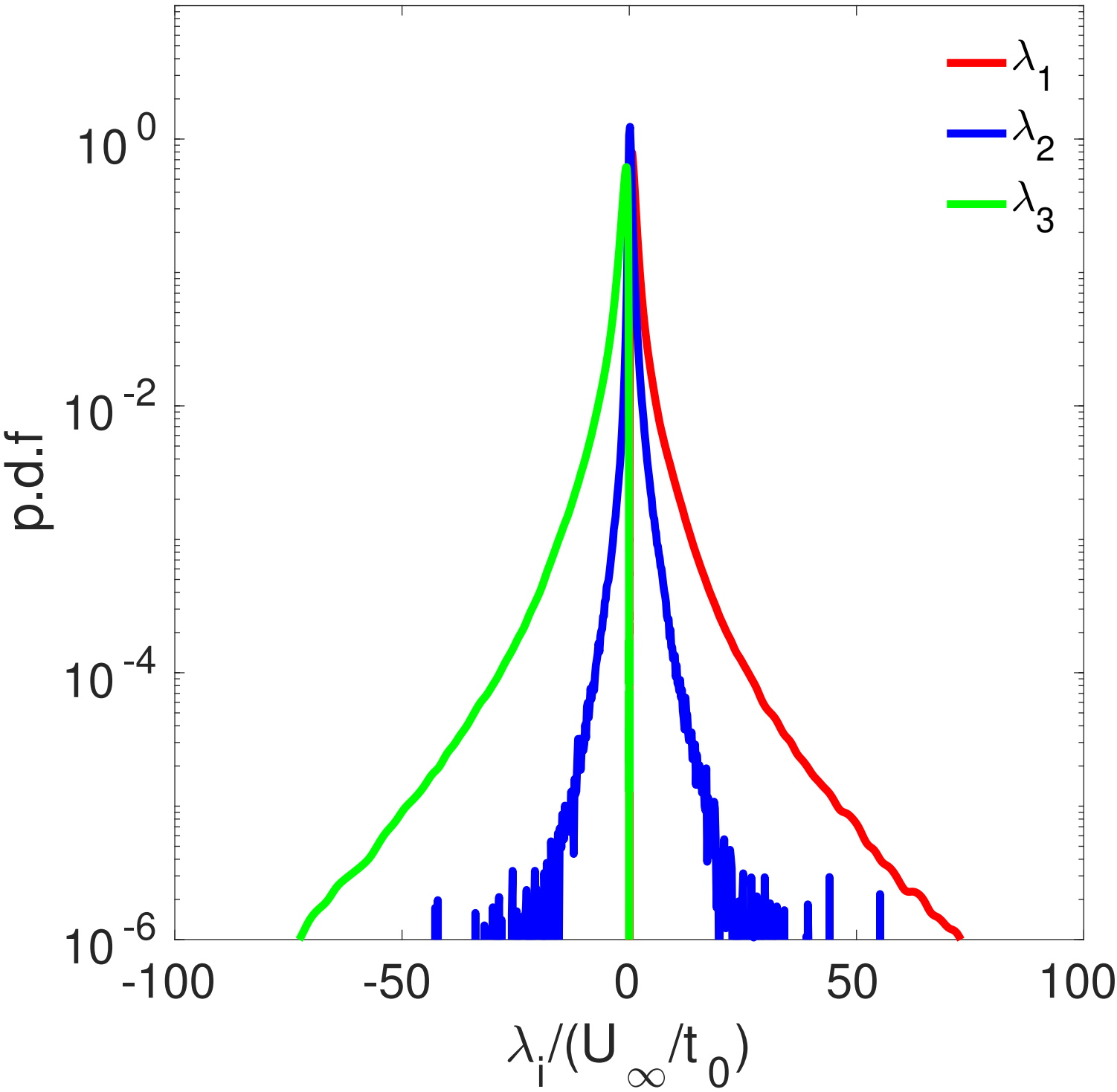

Accepted to Phys. Fluids 10.1063/5.0100334

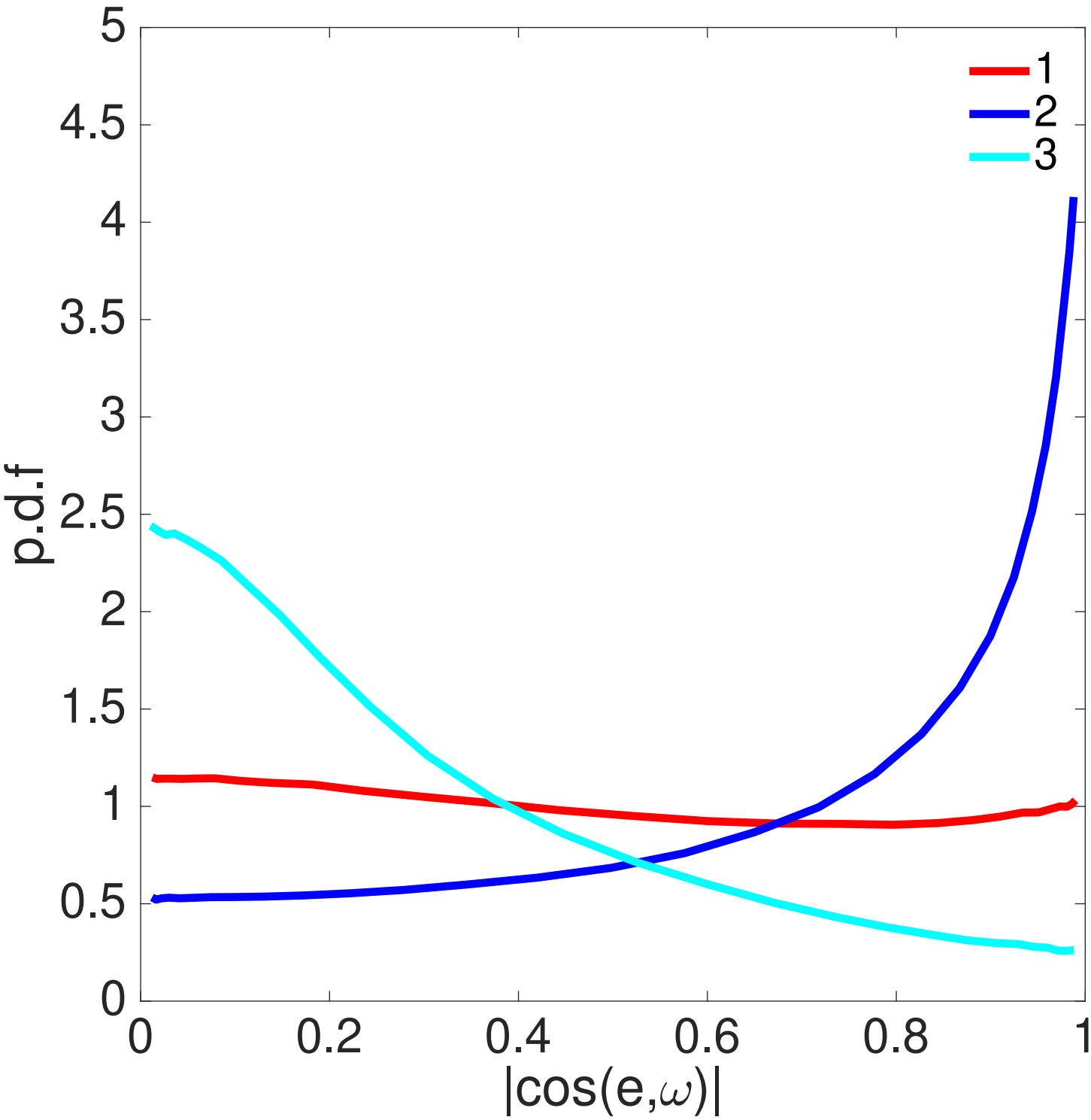

Accepted to Phys. Fluids 10.1063/5.0100334

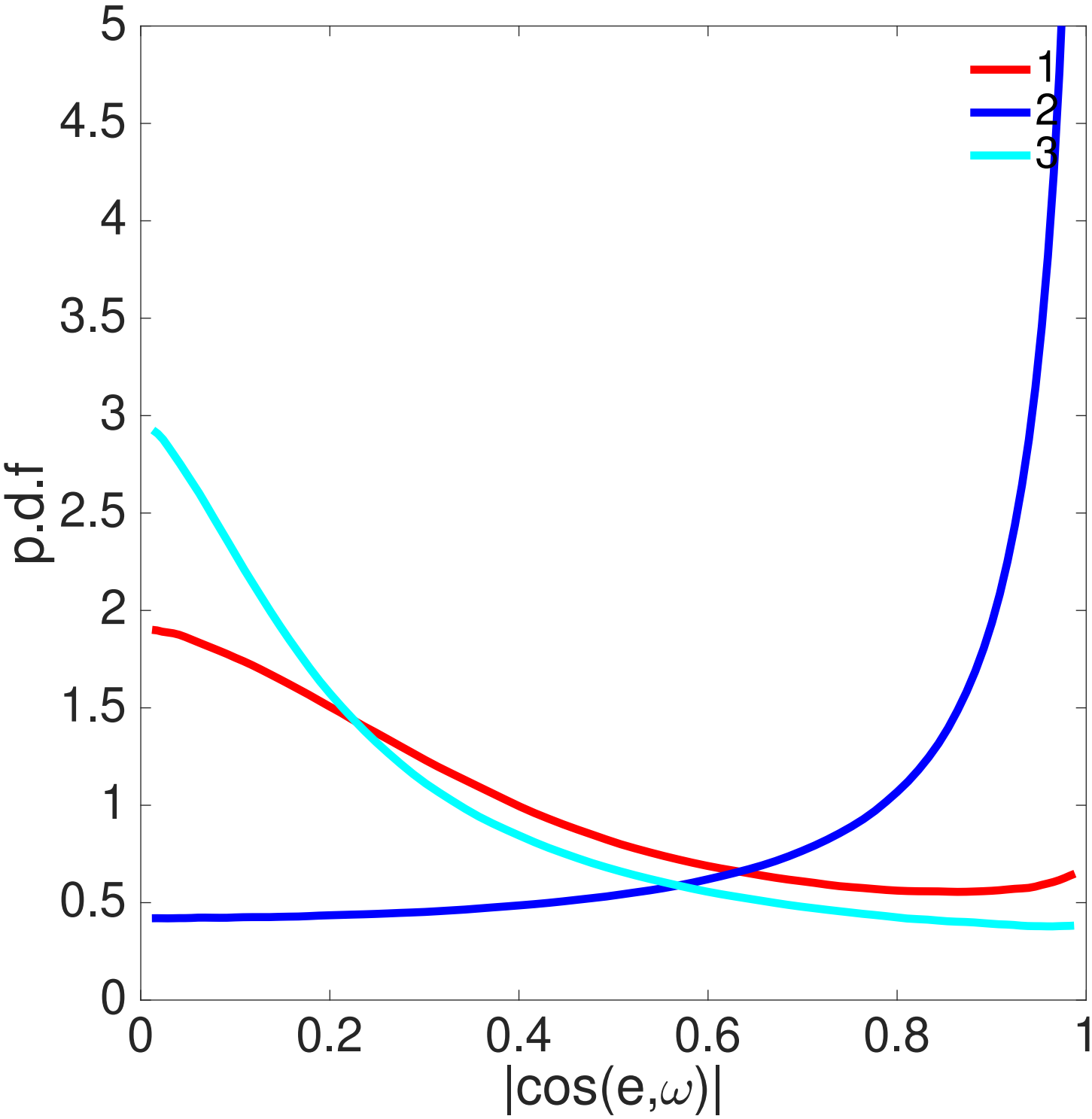

Accepted to Phys. Fluids 10.1063/5.0100334

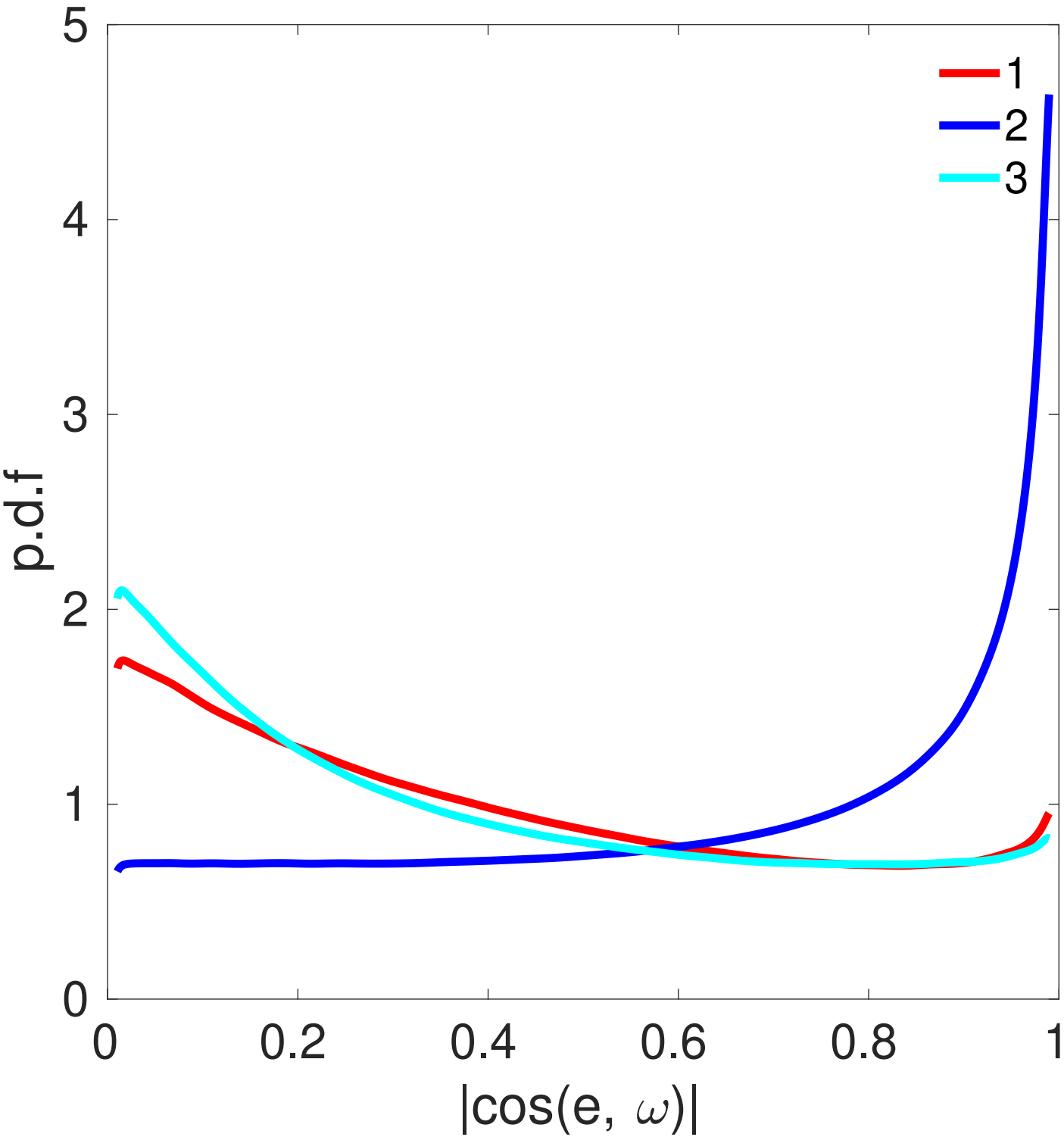

Accepted to Phys. Fluids 10.1063/5.0100334

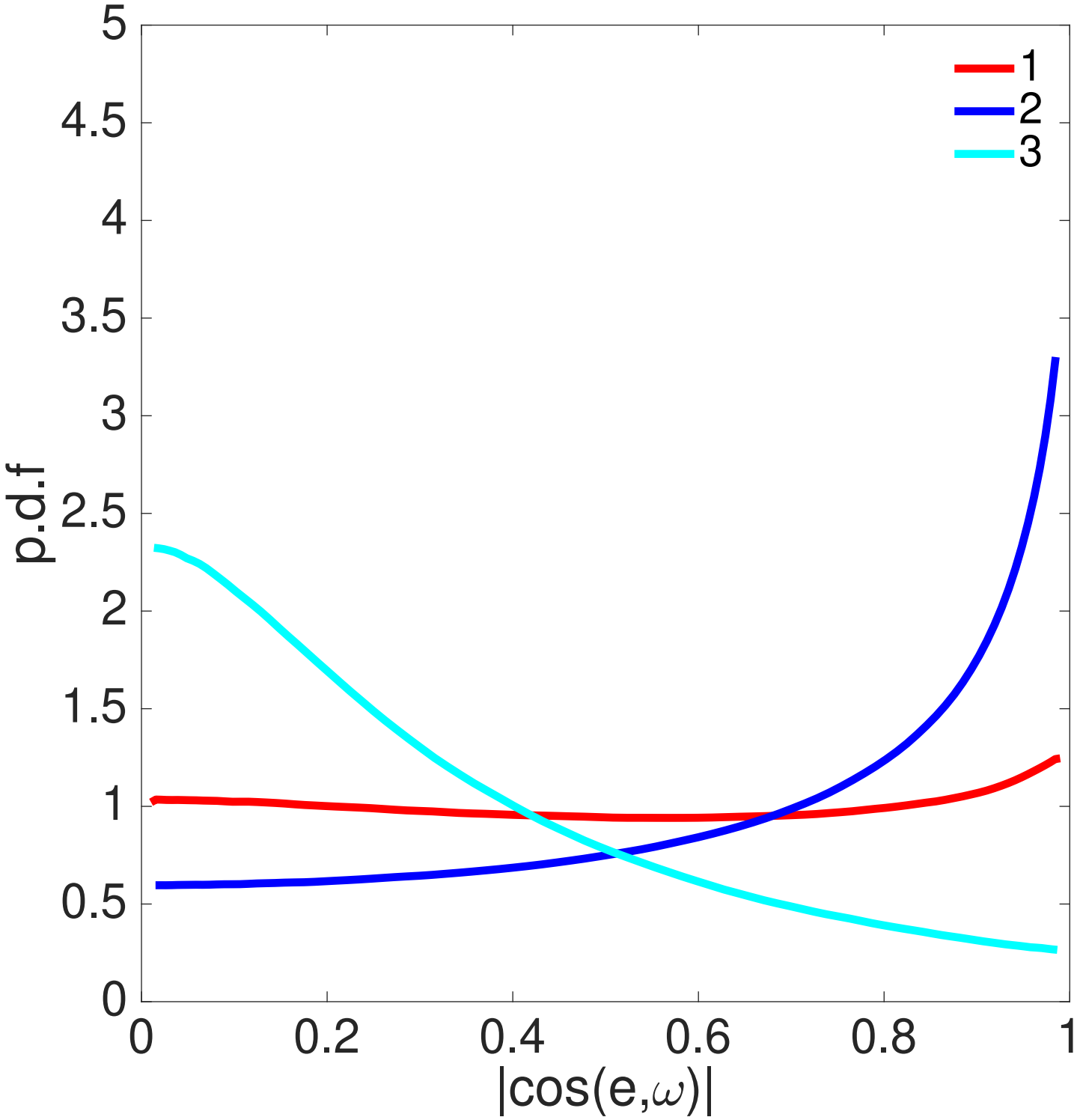
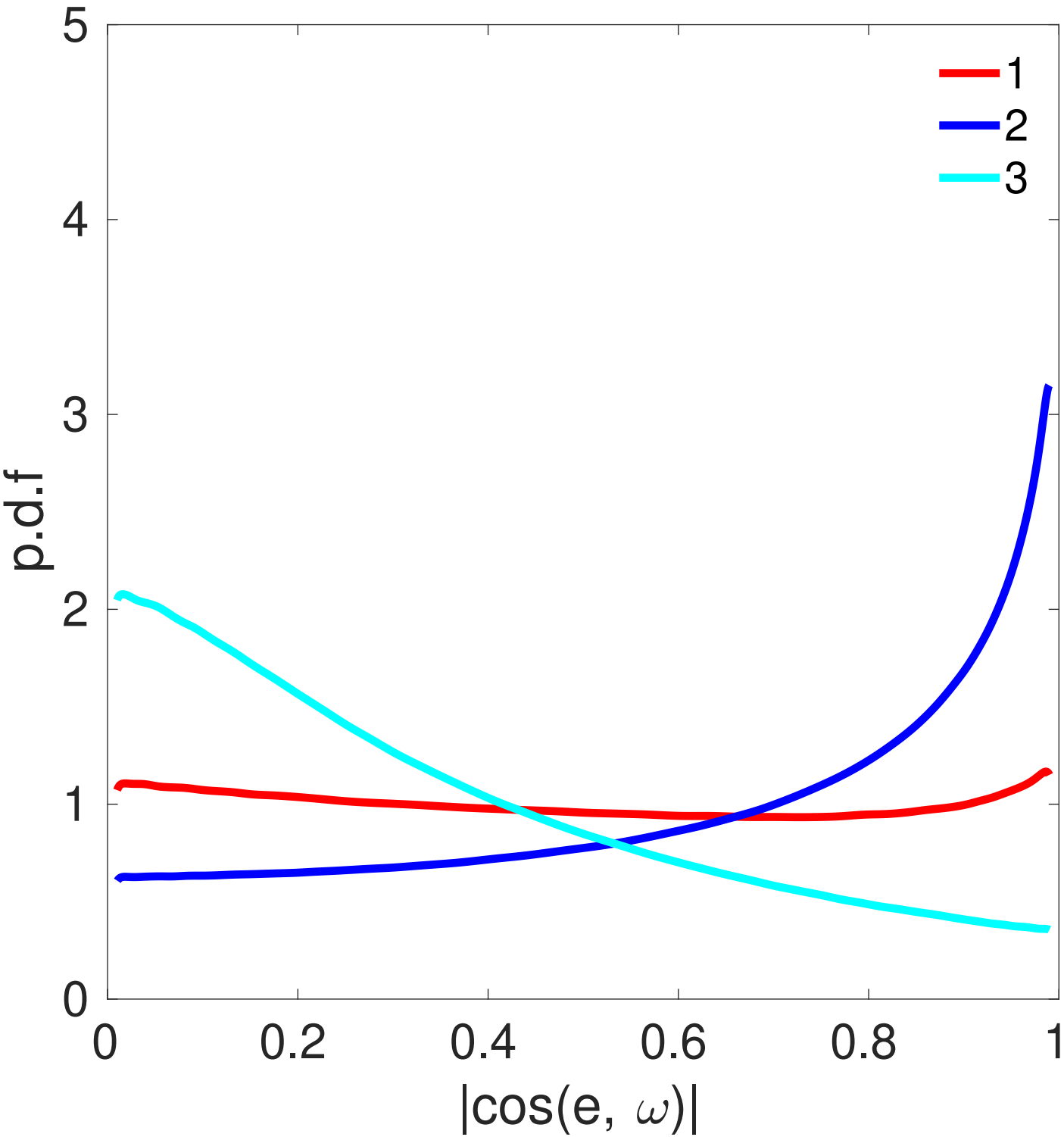
Accepted to Phys. Fluids 10.1063/5.0100334